Resonances of the InSight Seismometer on Mars

Kenneth Hurst, Lucile Fayon, Brigitte Knapmeyer-Endrun, Cedric Schmelzbach, Martin van Driel, Joan Ervin, Sharon Kedar, William Pike, Simon Calcutt, Tristram Warren, et al.

Resonances of the InSight Seismometer on Mars

K. J. Hurst[0], **L. Fayon**[2,9], **B. Knapmeyer-Endrun**[3], **C. Schmelzbach**[4], **M. van Driel**[4], **J. Ervin**[1], **S. Kedar**[1], **W. Pike**[5], **M. Bierwirth**[6], **P. Lognonne**[2], **S. Ceylan**[4], **M. Böse**[4], **J. Clinton**[4], **D. Giardini**[4], **A. Horleston**[8], **T. Kawamura**[2], **A. Khan**[4,11], **G. Orhand-Mainsant**[10], **J.-R. Scholz**[6], **S. Stähler**[4], **J. Stevanovic**[8,7], **W. Banerdt**[1]

[0]Corresponding author, Jet Propulsion Laboratory / California Institute of Technology, Ken.Hurst@jpl.nasa.gov

[1]Jet Propulsion Laboratory / California Institute of Technology

[2]Institut de Physique du Globe de Paris

[3]Bensberg Observatory, University of Cologne

[4]Eidgenössische Technische Hochschule Zürich

[5]Imperial College London

[6]Max Planck Institute for Solar System Research, Göttingen, Germany

[7]Now at AWE Blacknest

[8]University of Bristol

[9]Space Exploration Institute, Neuchâtel, Switzerland

[10]Institut Superieur l'Aéronautique et de l'Espace

[11]University of Zurich, Department of Physics, Zurich, Switzerland

Declaration of Competing Interests

The authors acknowledge there are no conflicts of interest recorded.

Abstract

The InSight seismometer was deployed to the surface of Mars in December 2018 - February 2019. The specific deployment conditions, which are very different from those of a standard broad-band instrument on Earth, result in resonances caused by different parts of the sensor

assembly, e.g. the leveling system or the load-shunt assembly on the tether connecting seismometer and lander, and recorded by the seismometer. Here, we present and characterize the resonances known to be present in the sensor assembly and their causes in order to aid interpretation of the seismic signals observed on Mars. Briefly, there are resonances in the sensor assembly at about 2.9, 5.3, 9.5, 12, 14, 23-28, and 51 Hz. We discuss various methods and tests that were used to characterize these resonances, and provide evidence for some of them in data collected on Mars. In addition to their relevance for the high-frequency analysis of seismic data from InSight, specifically for phase measurements near the resonant frequencies, the tests and observations described here are also of potential use in the further development of planetary seismometers, e.g. for Mars, the Moon, or Europa.

Introduction

The InSight mission to Mars (**In**terior Exploration using **S**eismic **I**nvestigations, **G**eodesy and **H**eat **T**ransport) carried, as its primary instrument, SEIS, a seismometer package consisting of two 3-component seismometers (Banerdt et al., 2020; Lognonné et al., 2020, 2019). Figure 1 shows the configuration of the major components as deployed on Mars. SEIS is deployed south of the lander (azimuth of 195^o), about 1.8m from the nearest lander foot. A cutaway of the sensor assembly that was deployed to the surface of Mars is shown in figure 2. An example of one Sol of seismic data as recorded on Mars is shown in figure 3.

When interpreting the signals recorded by a seismometer, it is important to understand which signals are not truly generated by physical processes exterior to the instrument. For planetary deployments, the harsh environment (e.g. huge temperature fluctuations) and the necessary proximity to artificial lander structures are important sources of non-seismic signals. For example, the Apollo seismometers recorded thermal cracking and gas venting from their lunar modules (Latham et al., 1970), thermal expansion and contraction of the Mylar shroud covering the sensors and their tether (Lammlein et al., 1974) as well as moonquakes. Various activities of the Viking 2 Martian lander, i.e. physical motions or electrical transients related to other experiments, were identified

in the seismometer recordings on that lander (Anderson et al., 1977). For InSight, seismic signals caused by typical lander activities as well as due to atmospheric effects and instrument crosstalk are described by Ceylan et al. (2021).

Properly distinguishing artificial disturbances from seismic signals is of special relevance in the case of InSight on Mars, where prior knowledge on typical seismic signals is poor and only recordings from a single station in a non-standard deployment situation, as compared to Earth, are available. Amplification of specific frequencies, i.e. resonances, is especially important when signal polarization or amplitude spectra are evaluated, e.g. to obtain information on subsurface structure from H/V ratios (Knapmeyer-Endrun et al., 2018). For the Moon, the amplification of signals on one of the horizontal components has been interpreted both as directivity related to structural complexity in H/V spectral ratios (Dal Moro, 2015), and as caused by a stiff connecting cable exiting the sensor assembly along the axis parallel to that component (Lammlein et al., 1974).

A detailed knowledge of resonances of the InSight seismometer is thus essential to correctly identify resonances caused by sub-surface structure. N. Dahmen led a paper in this special issue of BSSA that carried out an assessment of resonances between 1 to 9 Hz seen in the InSight seismic data. Many of the resonances identified therein (e.g. at 1.6 Hz, 2.7 Hz, 3.3 Hz, 3.7 Hz, 4.1 Hz, 4.2 Hz, 5.1 Hz, 5.2 Hz, 6.8 Hz, 7.8 Hz and 8.6 Hz) are assigned to the lander.

In this paper we describe the resonances within the SEIS sensor assembly. We will show that for frequencies below 10 Hz the resonances in the SEIS sensor assembly do not contaminate the data for most purposes. For frequencies above 20 Hz, we can sometimes see an effect on phase relationships between the various components.

The mission also deployed the Heat flow and Physical Properties Probe (HP^3) (Banerdt et al., 2020) to the surface about 1.2 meters east-northeast of the seismometer. The HP^3 includes a "mole" which is essentially a self-hammering nail that is intended to penetrate 3-5 meters into the regolith, dragging a line of temperature sensors behind it to measure the geothermal gradient. SEIS listens to the HP^3 hammering as a seismic source, hoping to ascertain information about the shallow geology underlying the landing site.

The InSight seismometer is described in detail in Lognonné et al. (2019). An abbreviated description is included here to allow the reader to understand the items and locations referenced when discussing the resonances of the seismometer.

The InSight seismometer sensor assembly (SA) is shown in Figure 2. It consists of a 3-component very broad band (VBB) oblique seismometer operating inside an evacuated container, a 3-component short period seismometer (SP) with each component housed in a separate enclosure, and the support and leveling structure (LVL) that is placed on the Martian regolith and levels the SA to permit the proper operation of the 6 seismic sensors. The SP sensors are bolted to the perimeter of the LVL. This entire structure, including the LVL, is enclosed inside a double-walled thermal enclosure known as the RWEB made of aluminized Kapton^{TM} supported by a titanium frame. Electrical power and signals go between the seismometer electronics housed in the InSight lander and the SA via a "tether" consisting of five 50 mm-wide flat belts of copper-on-Kapton^{TM} "flexprint". A wind and thermal shield (WTS) dome placed over the SA during the installation phase after verifying that the SA is properly set up provides a first line of isolation from the environment. A Load Shunt Assembly (LSA) mechanically disconnects the SA from thermoelastic disturbances originating in the tether and is also underneath the WTS.

In the following sections, we will first provide an overview of all the resonances observed in the InSight seismic data, and then delve more deeply into each resonance that originates in the SA. In this discussion, the SA includes all elements under the WTS, including the LSA. Then we will describe data collected on Mars relevant to the corresponding resonance. Finally, we will discuss the effect of all these resonances on the frequency response function for the sensor assembly. Spectral energy originating outside the SA, for example from vibrations of the InSight Lander, are outside the scope of this paper, and appropriate references are given with little to no discussion. In the supplemental material we describe Earth-based data collected before launch on the Flight Model (FM) and also data collected before and after launch on Engineering Models (EMs).

Overview of Resonances

The resonances below 10 Hz can be observed in the standard 20 samples per second (sps) continuous data. 100 sps event data specially downloaded for specified times of interest allow us to observe resonances up to 50 Hz. For signal content above 50 Hz, it is necessary to upload specialized filters to the seismometer and to engage in special analysis techniques. This is rarely done, and so far it has only been implemented during HP^3 mole hammering.

In the seismic data, the majority of resonance frequencies are observed to wander across the day, in general dropping in frequency slightly during the daytime, see figure 3.

Standard Operating Mode 1: up to 10 Hz (20 sps)

The VBB sensors are typically recorded at 20 sps for the velocity (VEL) outputs, and 1 sps for the position (POS) outputs. The SP sensors are typically recorded continuously at a rate of 100 sps. For much of the mission, the available bandwidth for sending data to Earth has permitted the VBB VEL and SP VEL to be downlinked at 20 sps and the VBB POS at 0.5 sps. At times of constrained bandwidth, particularly early in the mission, various lower rates were used for the continuous data. Late in the mission, the SP sensors were often turned off to conserve power as dust on the solar arrays progressively limited power generation. Ceylan et al. (2021) summarise the data availability in the first year of data collection.

While there is a spectral line at 1.00 Hz in both VBB and SP data, the origin of this line is in the electronics rather than in a mechanical resonance. It is described in Ceylan et al. (2021), and frequently avoided in standard data analysis such as shown in Figure 3.

There are no identified resonances attributed to SEIS below 1 Hz, and indeed none has so far been identified from any source.

Resonances at 2.9, 5.3, and 9.5 Hz were observed immediately following the adjustment of the pinning mass to open the LSA of the Tether during commissioning. They are discussed in the Tether section. These modes have highest amplitudes on the horizontal components rather than the vertical.

Resonances originating on the lander, several of which are prominent in the 1.6-10 Hz seismic data, are covered by a forthcoming paper by N. Dahmen et al.

There is a resonance visible at about 2.4 Hz in the Martian seismometer data. This mode is more dominant on the vertical component than it is on the horizontals (see Fig 3b). It is described and its origin, which as been the subject of some debate, is discussed in Ceylan et al. (2021); Clinton et al. (2021); Giardini et al. (2020). It does not originate in the sensor assembly.

Standard Operating Mode 2: up to 50 Hz (100 sps)

Based on the continuous data, the SEIS team can request episodes of the raw 100 sps SP data and the 1 Hz VBB POS data, provided it has not aged off the rotating buffer which lasts approximately 1 month.

Resonances at 12, 14, and 23-28 Hz were observed immediately following the adjustment of the pinning mass to open the LSA of the Tether during commissioning. They originate in the LSA and are discussed in the Tether section. These modes are seen largely in the horizontal components rather than the vertical.

Early in the commissioning activity, for a few sols right after the Sensor Assembly was placed on the Martian ground, there was a resonance in the LVL at about 39 Hz. One of the activities of the commissioning phase on Sol 44 was to retract all the legs of the LVL to lower the center of gravity and raise the resonant frequencies of the LVL system. As a result the 39 Hz resonance moved up to about 51 Hz (Fayon et al., 2018).

Special High Rate Operating Mode: above 50 Hz

The highest sampling rate at which SEIS can operate is 100 sps. Consequently, the highest nominal SEIS acquisition Nyquist frequency f_{Nyq} is 50 Hz. In conventional operation, information above 50 Hz is suppressed by a series of analog and digital anti-aliasing filters during data acquisition to ensure that no aliased information at frequencies larger than f_{Nyq} contaminates the 0 – 50 Hz frequency band of interest.

Two methods of collecting data on signals above 50 Hz by changing the anti-alias FIR filter in the data acquisition are described in detail in Sollberger et al. (2020). In support of using the HP^3 mole hammering as a seismic input signal, the digital (FIR) filters of the acquisition chain were changed during a few short time intervals to record information above f_{Nyq}.

The most prominent resonance observed above 50 Hz originates from the LVL. While the resonance of the LVL right after the deployment of SEIS on the Martian ground was observed at around 39 Hz, the resonance frequency increased to about 51 Hz after the LVL legs were retracted to bring the LVL to its current low position (Figure 4). Even though the resonant frequency increased by retracting the legs, the polarization pattern remained largely the same. This 51 Hz resonance has been interpreted by Fayon et al. (2018) and Lognonné et al. (2020) in terms of the stiffness of the interaction of the LVL feet with the regolith.

The Leveling System (LVL)

The LVL as mentioned earlier is a three-legged structure that supports all 6 components of the seismometer, and by extending or retracting the telescoping legs can level the sensors over a range of 15°(Lognonné et al., 2019). The ground on Mars where the seismometer was eventually deployed was within about 2.6°of level. Pictures of the LVL can be seen in Figures 2 and S5.

Very Broad Band (VBB) sensor and its supporting plate

The VBB sensors are oblique pendulums with a sensitivity axis inclined at about 30°to the horizontal (a true Galperin suspension would be at 35.26°). The natural period of each of the VBB pendulums was measured prior to launch, and most recently, on Mars as part of the commissioning early in the mission, and are in the vicinity of 0.5 Hz for all three sensors. Since the VBBs are operated in a force-feedback mode when collecting science data, this resonance is not seen in the seismic data. The VBB sensors can also operate in engineering mode without force-feedback, though this is rarely done. The structural supports and housing of the VBBs were designed to have

the lowest frequency normal mode above 100 Hz.

Short Period (SP) sensors

The SP sensor suite consists of one vertical and two horizontal MEMS (microelectromechanical systems) sensors. Details of their design and construction are given in Pike et al. (2018). The SP sensors have natural periods in the vicinity of 6 Hz. The SP sensors are also operated in a force-feedback mode when collecting science data, so this resonance is not seen in the seismic data either. Since the SP sensor housings are bolted directly to the main structure of the LVL, there are again no resonances below 100 Hz.

The Tether

The tether (Figure 5) provides electrical connectivity for power from the Lander to the SA, and analog signals from the Sensor Assembly to the SEIS Electronics Box (Ebox) in the Lander. It is composed of 5 belts of multi-layered copper and Kapton^{TM}, each about 0.5 mm thick and 50 mm wide. The belts are bundled with lacing at intervals, and are clamped together, among other places, at the LSA and the Pinning Mass.

The Pinning Mass provides the first line of isolation of the seismometer from disturbing forces generated in the tether. These forces can be caused by thermoelastic expansion and contraction of the tether as it goes across the ground from the lander to the SA. This portion of the tether is expected to see peak-to-peak diurnal temperature swings of 100^{o}C and 10-second fluctuations of 4^{o}C. Forces can also be generated by the wind, though given the very low density of the Martian atmosphere and the close proximity of the ground, these forces are small compared to the thermoelastic forces. The Pinning Mass also provides a "hook" which was used to adjust the opening of the LSA during deployment as shown in Figure 5 left side.

The LSA (Figure 5 right side, and Figure S5 right side) is a horseshoe-shaped section of the tether immediately outside the sensor assembly. When the WTS is placed over the SA, the LSA

is inside the WTS. It is created by heat-forming the tether in a special jig, and then is clamped in place by the LSA brackets. Its purpose is to decouple the sensor assembly from forces exerted by the tether. During launch, flight, and deployment, the LSA brackets are held together with a breakable bolt. After deployment, the bolt is broken and the LSA is adjusted such that the opposite sides of the horseshoe are not touching each other.

LSA: Characterization on Mars

The main opportunity to characterize the effect of the tether once deployed on Mars takes advantage of the opening of the LSA via the Pinning Mass adjustment as an external stimulation event.

Pinning Mass Adjustment

The Pinning Mass adjustment was an iterative process that occurred after the LSA frangibolt holding the two plates of the LSA bracket together had been released. The Lander's arm reached down, and with the tip of the scoop, drew the Pinning Mass toward the Lander a few cm per iteration. Figure 5 has an image from the deck-mounted context camera of the last move in progress on the left and an image from the arm-mounted camera showing the final configuration on the right.

Seismometer data collected during the last iteration provides an excellent way to characterize the normal modes of the open LSA, allowing us to estimate the frequencies, bandwidth, quality factor, polarization, and relative amplitudes of the different modes through spectral analysis of the oscillations and decay after the adjustment. Note that the estimation of the relative amplitudes is complicated by the faster decay of the higher frequencies. It is necessary to wait for the initial stimulus to be over, but if one waits too long the higher frequencies have decayed.

The very first attempt to move the Pinning Mass provides a way to assess the character of the LSA response for the brief time between the level-low operation of the SA (sol 44), and the inital opening of the LSA (sol 59). At this time, the frangibolt holding the two LSA plates together had been broken, however the spring force in the tether was still holding the two LSA plates in contact. The spectra for the radial, transverse (with respect to the tether direction), and vertical are shown

in Figure 6.

The spectra of the seismometer data taken during and immediately after the last pinning mass adjustment are shown in Figure 7. The data were sampled at 100 Hz. After removing the instrument response for displacement, they were rotated to radial = along the direction of the tether (15°azimuth on Mars), transverse = across the direction of the tether (285°azimuth on Mars), and vertical. From inspection of this spectra we derive the normal mode parameters in Table 1.

Polarization plots for each of the peaks in the spectra are shown in Figure 8. The 5.3 and 9.5 Hz resonances appear to result from linearly polarized near-horizontal motion. The other modes show varying levels of ellipticity. The 14 and 27 Hz resonances have similar polarization and may be multiples of each other, especially since the 27 Hz resonance is rather broad. The polarization of the 12 and 24 Hz resonances are different suggesting they are independent modes in spite of their relative frequencies.

Additional tests done on Earth to characterize the effect of the LSA are described in the supplemental material.

Examples of LSA Effect in Mars Seismic Data

An example of the effect of the LSA in seismometer data from Mars is provided in figure 9. This figure shows a histogram of the azimuth of the dominant polarization as a function of frequency for 5 minutes on 8 March 2019. In the vicinity of 25 Hz we see the strongest peaks at azimuths that correspond to the LSA transverse and radial directions. Furthermore, the polarization changes from LSA-radial to LSA-transverse at about 27 Hz, right where the LSA mode spectrum on the bottom suggests it should transition from radial to transverse dominance.

Another example of the effect of the LSA is shown in Figure 10. In this case, the 3 components of the SP data are being used to predict the VBB response. Residuals plotted in this case correspond to rotations of the sensor assembly around a vertical axis. In the left panel, all 3 SP components are used to create a filter to match the VBB-East component: $VBBE(f) = A(f) * SPZ(f) + B(f) * SPE(f) + C(f) * SPN(f)$ and the filter $|B(f)|$ is plotted. In the central panel, only the

SP-East component is used to create a filter to match the VBB-East component. $VBBE(f) = D(f) * SPE(f)$ and the filter $|D(f)|$ is plotted. The right panel shows $|B(f)/D(f)| - 1$ This shows a minor peak at 2.97 Hz, about 0.1 Hz above the frequency measured during the last pinning mass adjustment.

In general, it has been hard to identify other examples of the effect of the LSA on the seismic data. The lesson here is that care must be exercised when interpreting an analysis that is sensitive to phase relationships between the components near the resonant frequencies of the LSA.

Spring and Mass Models of the LSA

A simple harmonic oscillator with a spring and a mass has a frequency of $\omega = \sqrt{k/m}$, where k is the spring constant, and m is the mass. The lowest frequency LSA resonance is a radial mode at 2.9 Hz. The 9.5 Hz resonance is the lowest frequency resonance to be dominated by the component transverse to the tether. Given that the mass does not change, we can infer that the overall transverse spring constant of the LSA is $((9.5 * 2 * \pi)/(2.9 * 2 * \pi))^2 = 11$ times the radial spring constant. The spring constant of the LSA as inferred in this manner has a majority contribution from the interaction of the tether with the regolith outboard of the outer bracket. The seismometer would not see the contribution to the overall spring constant arising from the outboard regolith interaction.

An undamped coupled harmonic oscillator model of the seismometer and the LSA can help understand why evidence of the LSA modes is not easily found in the seismic data. Such a model is shown in Figure 11a. The LSA and the SEIS sensor assembly are coupled to the ground with springs having stiffness k_{2LSA} and k_{LVL} respectively. The LSA and the SEIS sensor assembly are coupled with a spring having stiffness k_{1LSA}. The mass of the SEIS sensor assembly was measured during integration into the spacecraft to be 8.8 kg. The mass of the LSA is configuration dependent. Based on photographs of the LSA taken just before the WTS was placed over it and mass properties measured prior to launch, we estimate the mass of the LSA to be 0.07 kg with about a 30% uncertainty. Given these masses and the relevant frequencies, we can calculate the

associated stiffnesses k. The stiffness for the LSA calculated in such a way is actually the sum of two stiffnesses, k_{1LSA} and k_{2LSA}. The stiffness k_{1LSA} should be the smaller of the two because the lengths of the arms of the LSA horseshoe bend are generally longer than the length of the tether from the LSA to the ground, again with the caveat that the LSA-ground length is configuration dependent. In our model, we will assume that $k_{1LSA} = k_{2LSA}$ as a likely worst case.

To build our understanding of the system, we first look at the 2.86 Hz fundamental mode and examine the case where the initial conditions are such that at t=0 we impart a displacement of 1.0e-6 m to the LSA only. This case is shown in figure 11b. The pinning mass adjustment described above is an example wherein the stimulus was largely to the LSA. In the top panel we see the LSA displacement respond with the expected sinusoidal displacement. In the middle panel we see the displacement response of the seismometer. We can observe both the 2.86 Hz signature of the LSA pushing and pulling on the sensor assembly but with an amplitude that is about 1e-5 less. This reduction in amplitude is due to a combination of the ratio of the sensor assembly mass of 8.8 kg, versus the LSA mass of 0.07 kg and the ratio of the stiffnesses of the sensor assembly to ground k_{LVL} versus the LSA to the sensor assembly k_{1LSA}. We also see a 51 Hz response of the sensor assembly superimposed on the 2.86 Hz response. The power spectrum in the bottom panel shows that the power at 51 Hz is the same as at 2.86 Hz. Our first lesson is then that the motion input to the LSA is strongly attenuated by about 5 orders of magnitude in the SEIS response. This is in agreement with the experiment described in the suplemental material figures S2 and S3.

We then turn our attention to figure 11c, to understand the effect of the LSA to an input signal common to both the LSA and the seismometer. In this case we impose an initial condition at t=0 of the same 1.0e-6 m displacement to both the sensor assembly and to the LSA. In the top panel we once again see the expected 2.86 Hz sinusoidal displacement response of the LSA. In the middle panel we see the expected 51 Hz sinusoidal displacement response of the sensor assembly. The power spectrum in the bottom panel shows that the LSA effect on the seismometer is appearing at the expected 2.86 Hz, but with a power that is about seven orders of magnitude less than the primary SEIS response at 51 Hz. At these levels, it is very hard to identify the effect of the LSA in

typical seismic data. It is possible for the LSA to have a measurable effect on phase measurements near the resonant frequencies however as seen in figures 9 and 10.

This analysis is for linear displacement motion of the tether. Other investigations involving rotational modes are ongoing.

Conclusion

The SEIS Sensor Assembly has no resonances below 1 Hz. Above 1 Hz, there are a number of resonances at about 2.86, 5.3, 9.5, 12, 14, 23-28, and 51 Hz. A transfer function is well approximated with a horizontal line at 1.0 from 0.04 to 1 Hz. Much work has gone into understanding arrivals in the 1-10 Hz range in the Mars seismic data so far. The results reported in this paper demonstrate that the resonances in the sensor assembly do not affect the recorded spectra, however special attention should be given to any observations relying on phase relationships at frequencies near the LSA resonances.

Data and Resources

InSight seismic data is available from the Planetary Data System (PDS) and from InSight Mars SEIS Data Service. https://doi.org/10.18715/SEIS.INSIGHT.XB_2016

The laboratory test data that is not part of the InSight mission data repository is available from JPL-ARCHIVE-XXX (JPL library will provide a doi.)

Acknowledgements

A portion of the work was supported by the InSight Project at the Jet Propulsion Laboratory (JPL), California Institute of Technology, under a contract with the National Aeronautics and Space Administration (NASA). We acknowledge NASA; CNES (Centre Nationale d'Etudes Spatiale); their partner agencies and Institutions UKSA (United Kingdom Space Agency), SSO (Swiss Space Office), DLR (Deutsches Zentrum fur Luft- und Raumfahrt), JPL, IPGP-CNRS (Institute de Physique

du Globe de Paris-Centre National de la Recherche Scientifique), ETHZ (Eidgenössische Technische Hochschule Zurich), IC (Imperial College), MPS-MPG (Max Planck Institute for Solar System Research-Max Planck Gesellschaft); INTA/CSIC-CAB (Instituto Nacional de Técnica Aeroespacial/Consejo Superior de Investigaciones Científicas-Centro Astrobioligía); and the flight operations team at JPL, SISMOC (SEIS on Mars Operations Center), MSDS (Mars SEIS Data Service), IRISDMC (Incorporated Research Institutions for Seismology-Data Management Center) and PDS (Planetary Data Service) for providing the SEED (Standard for the Exchange of Earthquake Data) SEIS data used. French co-authors acknowledge the French Space Agency CNES, CNRS and ANR (Agence Nationale pour la Recherche) (ANR-10-LABX-0023, ANR-11-IDEX-0005-0). The Swiss co-authors were jointly funded by the Swiss National Science Foundation (SNF-ANR project 157133), the Swiss State Secretariat for Education, Research and Innovation (SEFRI project "MarsQuake Service-Preparatory Phase") and ETH Research grant ETH-06 17-02.

Some of the analysis used in this paper used the ObsPy software package Beyreuther et al. (2010).

We acknowledge NASA, CNES, their partner agencies and Institutions (UKSA, SSO, DLR, JPL, IPGP-CNRS, ETHZ, IC, MPS-MPG) and the flight operations team at JPL, SISMOC, MSDS, IRIS-DMC and PDS for providing SEED SEIS data.

InSight contribution number 142.

References

Anderson, D. L., W. F. Miller, G. V. Latham, Y. Nakamura, M. N. Toksöz, A. M. Dainty, F. K. Duennebier, A. R. Lazarewicz, R. L. Kovach, and T. C. D. Knight (1977). Seismology on mars. *Journal of Geophysical Research 82*, 4524–4546.

Banerdt, W. B., S. E. Smrekar, D. Banfield, D. Giardini, M. Golombek, C. L. Johnson, P. Lognonné, A. Spiga, T. Spohn, C. Perrin, et al. (2020). Initial results from the insight mission

on mars. *Nature Geoscience 13*(3), 183–189.

Beyreuther, M., R. Barsch, L. Krischer, T. Megies, Y. Behr, and J. Wassermann (2010). Obspy: A python toolbox for seismology. *Seismological Research Letters 81*(3), 530–533.

Ceylan, S., J. F. Clinton, D. Giardini, M. Böse, C. Charalambous, M. van Driel, A. Horleston, T. Kawamura, A. Khan, G. Orhand-Mainsant, J.-R. Scholz, S. C. Stähler, F. Euchner, W. B. Banerdt, P. Lognonné, D. Banfield, E. Beucler, R. F. Garcia, S. Kedar, M. P. Panning, W. T. Pike, S. E. Smrekar, A. Spiga, N. L. Dahmen, K. Hurst, A. E. Stott, R. D. Lorenz, M. Schimmel, E. Stutzmann, J. t. Pierick, V. Conejero, C. Pardo, and P. Clément (2021). Companion guide to the marsquake catalog from insight, sols 0–478: Data content and non-seismic events. *Physics of the Earth and Planetary Interiors 310*, 106597.

Clinton, J., D. Giardini, M. Böse, S. Ceylan, M. van Driel, F. Euchner, R. F. Garcia, S. Kedar, A. Khan, S. C. Stähler, et al. (2018). The marsquake service: Securing daily analysis of seis data and building the martian seismicity catalogue for insight. *Space Science Reviews 214*(8), 1–33.

Clinton, J. F., S. Ceylan, M. van Driel, D. Giardini, S. C. Stähler, M. Böse, C. Charalambous, N. L. Dahmen, A. Horleston, T. Kawamura, et al. (2021). The marsquake catalogue from insight, sols 0–478. *Physics of the Earth and Planetary Interiors 310*, 106595.

Dal Moro, G. (2015). Joint analysis of rayleigh-wave dispersion and HVSR of lunar seismic data from the Apollo 14 and 16 sites. *Icarus 254*, 338–349.

Fayon, L., B. Knapmeyer-Endrun, P. Lognonné, M. Bierwirth, A. Kramer, P. Delage, F. Karakostas, S. Kedar, N. Murdoch, R. F. Garcia, N. Verdier, S. Tillier, W. T. Pike, K. Hurst, C. Schmelzbach, and W. B. Banerdt (2018, Oct). A numerical model of the seis leveling system transfer matrix and resonances: Application to seis rotational seismology and dynamic ground interaction. *Space Science Reviews 214*(8), 119.

375 Giardini, D., P. Lognonné, W. B. Banerdt, W. T. Pike, U. Christensen, S. Ceylan, J. F. Clinton,
376 M. van Driel, S. C. Stähler, M. . Böse, K. Hurst, et al. (2020). The seismicity of mars. *Nature*
377 *Geoscience 13*(3), 205–212.

378 Kedar, S., W. Banerdt, N. Brinkman, P. Delage, L. Fayon, M. Grott, A. Horleston, T. Hudson,
379 K. Hurst, A. Kiely, et al. (2019). Characterization of the insight near surface seismic properties
380 using the heat flow and physical properties probe (hp3) mole as a seismic source. In *Lunar and*
381 *Planetary Science Conference*, Volume 50.

382 Knapmeyer-Endrun, B., N. Murdoch, B. Kenda, M. P. Golombek, M. Knapmeyer, L. Witte,
383 N. Verdier, S. Kedar, P. Lognonné, and W. B. Banerdt (2018). Influence of body waves, instru-
384 mentation resonances, and prior assumptions on rayleigh wave ellipticity inversion for shallow
385 structure at the insight landing site. *Space Science Reviews 214*(5), 94.

386 Lammlein, D. R., G. V. Latham, J. Dorman, Y. Nakamura, and M. Ewing (1974). Lunar seismicity,
387 structure, and tectonics. *Reviews of Geophysics 12*(1), 1–21.

388 Latham, G. V., M. Ewing, F. Press, G. Sutton, J. Dorman, Y. Nakamura, N. Toksöz, R. Wiggins,
389 J. Derr, and F. Duennebier (1970). Passive seismic experiment. *Science 167*(3918), 455–457.

390 Lognonné, P., W. Banerdt, W. Pike, D. Giardini, U. Christensen, R. Garcia, T. Kawamura, S. Kedar,
391 B. Knapmeyer-Endrun, L. Margerin, ..., and K. o. Hurst (2020). Constraints on the shallow
392 elastic and anelastic structure of mars from insight seismic data. *Nature Geoscience 13*(3),
393 213–220.

394 Lognonné, P., W. B. Banerdt, D. Giardini, W. T. Pike, U. Christensen, P. Laudet, S. de Raucourt,
395 P. Zweifel, S. Calcutt, M. Bierwirth, K. J. Hurst, F. Ijpelaan, J. W. Umland, R. Llorca-Cejudo,
396 S. A. Larson, R. F. Garcia, S. Kedar, B. Knapmeyer-Endrun, D. Mimoun, A. Mocquet, M. P. Pan-
397 ning, R. C. Weber, A. Sylvestre-Baron, G. Pont, N. Verdier, L. Kerjean, L. J. Facto, V. Gharaka-
398 nian, J. E. Feldman, T. L. Hoffman, D. B. Klein, K. Klein, N. P. Onufer, J. Paredes-Garcia,
399 M. P. Petkov, J. R. Willis, S. E. Smrekar, M. Drilleau, T. Gabsi, T. Nebut, O. Robert, S. Tillier,

C. Moreau, M. Parise, G. Aveni, S. Ben Charef, Y. Bennour, T. Camus, P. A. Dandonneau, C. Desfoux, B. Lecomte, O. Pot, P. Revuz, D. Mance, J. tenPierick, N. E. Bowles, C. Charalambous, A. K. Delahunty, J. Hurley, R. Irshad, H. Liu, A. G. Mukherjee, I. M. Standley, A. E. Stott, J. Temple, T. Warren, M. Eberhardt, A. Kramer, W. Kühne, E.-P. Miettinen, M. Monecke, C. Aicardi, M. André, J. Baroukh, A. Borrien, A. Bouisset, P. Boutte, K. Brethomé, C. Brysbaert, T. Carlier, M. Deleuze, J. M. Desmarres, D. Dilhan, C. Doucet, D. Faye, N. Faye-Refalo, R. Gonzalez, C. Imbert, C. Larigauderie, E. Locatelli, L. Luno, J.-R. Meyer, F. Mialhe, J. M. Mouret, M. Nonon, Y. Pahn, A. Paillet, P. Pasquier, G. Perez, R. Perez, L. Perrin, B. Pouilloux, A. Rosak, I. Savin de Larclause, J. Sicre, M. Sodki, N. Toulemont, B. Vella, C. Yana, F. Alibay, O. M. Avalos, M. A. Balzer, P. Bhandari, E. Blanco, B. D. Bone, J. C. Bousman, P. Bruneau, F. J. Calef, R. J. Calvet, S. A. D'Agostino, G. de los Santos, R. G. Deen, R. W. Denise, J. Ervin, N. W. Ferraro, H. E. Gengl, F. Grinblat, D. Hernandez, M. Hetzel, M. E. Johnson, L. Khachikyan, J. Y. Lin, S. M. Madzunkov, S. L. Marshall, I. G. Mikellides, E. A. Miller, W. Raff, J. E. Singer, C. M. Sunday, J. F. Villalvazo, M. C. Wallace, D. Banfield, J. A. Rodriguez-Manfredi, C. T. Russell, A. Trebi-Ollennu, J. N. Maki, E. Beucler, M. Böse, C. Bonjour, J. L. Berenguer, S. Ceylan, J. Clinton, V. Conejero, I. Daubar, V. Dehant, P. Delage, F. Euchner, I. Estève, L. Fayon, L. Ferraioli, C. L. Johnson, J. Gagnepain-Beyneix, M. Golombek, A. Khan, T. Kawamura, B. Kenda, P. Labrot, N. Murdoch, C. Pardo, C. Perrin, L. Pou, A. Sauron, D. Savoie, S. Stähler, E. Stutzmann, N. A. Teanby, J. Tromp, M. van Driel, M. Wieczorek, R. Widmer-Schnidrig, and J. Wookey (2019, Jan). Seis: Insight's seismic experiment for internal structure of mars. *Space Science Reviews 215*(1), 12.

Lognonné, P., W. B. Banerdt, W. T. Pike, D. Giardini, D. Banfield, U. Christensen, M. Bierwirth, S. S Calcutt, J. Clinton, S. Kedar, et al. (2019). Seis: Overview, deployment, and first science on the ground. In *Lunar and Planetary Science Conference*, Volume 50.

Pavlis, G. L. and F. L. Vernon (1994). Calibration of seismometers using ground noise. *Bulletin of the seismological society of America 84*(4), 1243–1255.

426 Peters, G. H., W. Abbey, G. H. Bearman, G. S. Mungas, J. A. Smith, R. C. Anderson, S. Douglas,
427 and L. W. Beegle (2008). Mojave mars simulant—characterization of a new geologic mars
428 analog. *Icarus 197*(2), 470–479.

429 Peterson, J. R. (1993). Observations and modeling of seismic background noise. Technical report,
430 US Geological Survey.

431 Pike, W., I. Standley, S. Calcutt, and A. Mukherjee (2018). A broad-band silicon microseismometer
432 with 0.25 ng/rthz performance. In *2018 IEEE Micro Electro Mechanical Systems (MEMS)*, pp.
433 113–116. IEEE.

434 Scholz, J.-R., R. Widmer-Schnidrig, P. Davis, P. Lognonné, B. Pinot, R. F. Garcia, K. Hurst, L. Pou,
435 F. Nimmo, S. Barkaoui, et al. (2020). Detection, analysis, and removal of glitches from insight's
436 seismic data from mars. *Earth and Space Science 7*(11), e2020EA001317.

437 Sollberger, D., C. Schmelzbach, F. Andersson, J. O. Robertsson, N. Brinkman, S. Kedar,
438 B. Banerdt, J. Clinton, M. van Driel, R. F. Garcia, et al. (2020). A reconstruction algorithm
439 for temporally aliased seismic signals recorded by the insight mars lander. *Earth and Space*
440 *Science Open Archive ESSOAr 0*, 1–42.

Author addresses

K. J. Hurst; MS 264-500, Jet Propulsion Laboratory, Pasadena CA USA 91109;
Ken.Hurst@jpl.nasa.gov
L. Fayon; Rue de Pain Blanc 17, 2000 Neuchâtel Switzerland; Fayon@ipgp.fr,
B. Knapmeyer-Endrun; Bensberg Observatory, University of Cologne, Vinzenz-Pallotti-Str. 26,
51429 Bergisch Gladbach, Germany; brigitte.knapmeyer-endrun@uni-koeln.de
C. Schmelzbach; Soneggstrasse 5, Zurich 8092, Switzerland; Cedric.schmelzbach@erdw.ethz.ch
M. van Driel; Soneggstrasse 5, Zurich 8092, Switzerland; vandriel@erdw.ethz.ch
J. Ervin; MS 321-400 Jet Propulsion Laboratory, Pasadena CA USA 91109;
joan.ervin@jpl.nasa.gov
S. Kedar; MS 238-600 Jet Propulsion Laboratory, Pasadena CA USA 91109;
sharon.kedar@jpl.nasa.gov
W. Pike; South Kensington Campus London SW7 2AZ, UK; w.t.pike@imperial.ac.uk
M. Bierwirth; Max-Planck-Institute for Solar System Research. Justus-von-Liebig Weg 3,
D-37077 Göttingen, Germany; bierwirthm@mps.mpg.de
P. Lognonne; IPGP - 1, rue Jussieu - 75238 Paris cedex 05; lognonne@ipgp.fr
S. Ceylan; Soneggstrasse 5, Zurich 8092, Switzerland; savas.ceylan@erdw.ethz.ch
M. Böse; Soneggstrasse 5, Zurich 8092, Switzerland; mboese@sed.ethz.ch
J. Clinton; Soneggstrasse 5, Zurich 8092, Switzerland; jclinton@sed.ethz.ch
D. Giardini; Soneggstrasse 5, Zurich 8092, Switzerland; domenico.giardini@erdw.ethz.ch
A. Horleston; School of Earth Sciences, University of Bristol, Will's Memorial Building,
Queen's Road, Bristol, BS8 1RJ, UK; Anna.Horleston@bristol.ac.uk
T. Kawamura; IPGP - 1, rue Jussieu - 75238 Paris cedex 05; kawamura@ipgp.fr
A. Khan; Soneggstrasse 5, Zurich 8092, Switzerland; amir.khan@erdw.ethz.ch
G. Orhand-Mainsant; 10 Avenue Edouard Belin, 31055 Toulouse, France;
guenole.mainsant@outlook.fr
J. R. Scholz; Max-Planck-Institute for Solar System Research. Justus-von-Liebig Weg 3,

D-37077 Göttingen, Germany scholz@mps.mpg.de

S. Stähler; Soneggstrasse 5, Zurich 8092, Switzerland; simon.staehler@erdw.ethz.ch

J. Stevanovic; AWE Blacknest, Brimpton, Reading, Berkshire, RG7 4RS United Kingdom; jenny@blacknest.gov.uk

W. Banerdt; 1202 Arch St., Pittsburgh, PA 15212; william.b.banerdt@jpl.nasa.gov

Tables

Table 1: Relative displacement amplitudes, Q factors, and bandwidths of the normal modes of the open LSA taken from seismometer data collected during and just after the final Pinning Mass adjustment on Mars. R == radial with respect to the direction of the tether. T == transverse to the tether. Z == Vertical. The amplitudes have been normalized such that the 2.86 Hz resonance relative amplitude is 1.0. Note that the estimation of the relative amplitudes is complicated by the faster decay of the higher frequencies.

Hz	Radial			Transverse			Vertical		
	Rel Amp	Q	BW(Hz)	Rel Amp	Q	BW(Hz)	Rel Amp	Q	BW(Hz)
2.9	1.0	23	0.13	0.63	23	0.13	0.20	15	0.13
5.3	0.59	35	0.15	0.30	35	0.15	0	NA	NA
9.5	0.41	13	0.76	0.58	14	0.70	0.14	14	0.70
12	0.20	21	0.58	0.22	25	0.48	0	NA	NA
14	0.09	70	0.20	0.19	74	0.19	0.03	66	0.21
23-28	NA	NA	NA	NA	NA	NA	NA	NA	NA

List of figure captions

Figure 1: The InSight lander viewed from the south. (Artists conception) The seismic sensors in the Sensor Assembly receive power from, and send signals to, the SEIS electronics housed in the Lander, where they are kept much warmer, via the tether. The Heat Flow and Physical Properties Package (HP^3) experiment is on the ground to the right of SEIS, and the Instrument Deployment Arm (IDA) with attached Camera used to deploy both the SEIS Sensor Assembly and the HP^3 probe is above the lander.

Figure 2: Cutaway view of the InSight seismometer sensor assembly on Mars. RWEB: double-walled thermal enclosure. WTS: Wind and Thermal Shield. LVL: One leveling leg (of 3) for the leveling and support structure. SP sensor: One of 3 SP sensors (this one is the vertical one). VBB sensor: One of 3 oblique VBB sensors inside the evacuated chamber. LSA: Load Shunt Assembly (shown prior to opening) to isolate the thermoelastic disturbances in the tether from the sensor assembly. Tether: A five-belt copper-on-Kapton flexible circuit connecting the sensor assembly to the electronics in the lander. PM: Pinning Mass helps isolate the thermoelastic disturbances in the tether from the sensor assembly, and provides a handle for adjusting the opening of the LSA.

Figure 3: Example of typical data from Sol 348: vertical acceleration time series and vertical and north spectrograms from (a) 100 sps SP, and (b) 20 sps VBB. The x-axes at the bottom shows time in both UTC and Local Mean Solar Time on Mars as LMST. Sunrise and sunset are shown as orange hemispheres with arrows at the top of the panels,and as orange circles in the timescale at the bottom. To the right of the spectrograms are the probabilistic power spectral density. At the top, there are two filtered versions of the time series (above and below 1Hz). The strongest horizontal lines in the spectrogram between 2 and 10 Hz are traceable to the lander and are discussed in Ceylan et al. (2021). The many vertical "spikes" in (b) that appear to originate in the longest periods in the spectrogram are discussed in Scholz et al. (2020). The vertical purple bars in the waveform panels mark the duration of seismic events identified by the Marsquake Service Clinton et al. (2018).

Figure 4: Display of the azimuth of the major axis of the polarization ellipse with frequency and

time for wind induced noise for (a) Pre- and (b) post-leveling low of the LVL. The pre-leveling low LVL resonance at around 39 Hz was not as clearly visible as after leveling low, when the LVL resonance moved to 51 Hz, as suggested by the common azimuth of the pre- and post-leveling low resonances at around 60 degrees.

Figure 5: Context (left) and Deployment (right) Camera images of the last adjustment of the Pinning Mass to open the LSA. The shadow of the LSA in the Deployment image shows clearly that sunlight is able to shine all the way through, offering an additional avenue for assessing the proper state of the LSA opening.

Figure 6: Spectra of the LSA on Mars as stimulated by the first Pinning Mass adjustment during deployment. This is applicable to the period from sol 44 (leveling low) to sol 59 (LSA open). R == radial with respect to the direction of the tether. T == transverse to the tether. Z == Vertical.

Figure 7: Spectrograms of the LSA on Mars as stimulated by the last Pinning Mass adjustment during deployment. The data was high-pass filtered with a cutoff at 0.5 Hz. This is applicable from sol 59 (LSA open) to the end of the mission. R == radial with respect to the direction of the tether. T == transverse to the tether. Z == Vertical. The spectrum on the bottom right corresponds to a slice through the spectrogram at the white line in each spectrogram.

Figure 8: Polarization plots for the first 7 modes from the last pinning mass adjustment. The views are from 3 orthogonal viewpoints, with the left (map) view in map coordinates with North at 0°, and East at 90°. The middle plot is the N-V plane as viewed from the East, with up at 90°. And the right plot is the E-V plane as viewed from the South, again with up at 90°. The azimuth of the tether is at 15°and is indicated by the red arrows on the Map view plots. The narrow band-pass filters applied to isolate each mode are given in the titles for each set of plots.

Figure 9: Azimuthal histogram of 5 minutes of 100sps SP data from 8 March 2019, demonstrating the effect of resonances in the LSA between 23 and 28 Hz.

Figure 10: Residual from filtering the SP data to match the VBB data. In the left panel, all 3 SP components are used to create a filter to match the VBB-East component. In the central panel, only the SP-East component is used to create a filter to match the VBB-East component. The right panel

shows the ratio between the east component of the 3-component filter, and the single component filter. This shows a minor peak at 2.97 Hz, about 0.1 Hz above the frequency measured during the last pinning mass adjustment.

Figure 11: Coupled undamped harmonic oscillator model for SEIS Sensor Assembly and the LSA. a) A diagram of the model. b) Displacement response of the system to an initial displacement of only the LSA of 1.0e-6 m for the 2.86 Hz LSA resonance. c) Displacement response of the system to an initial displacement of **both** the Sensor Assembly and the LSA of 1.0e-6 m/s for the 2.86 Hz LSA resonance. The 2.86 Hz resonance can just be seen in the blowup in the PSD.

Figures

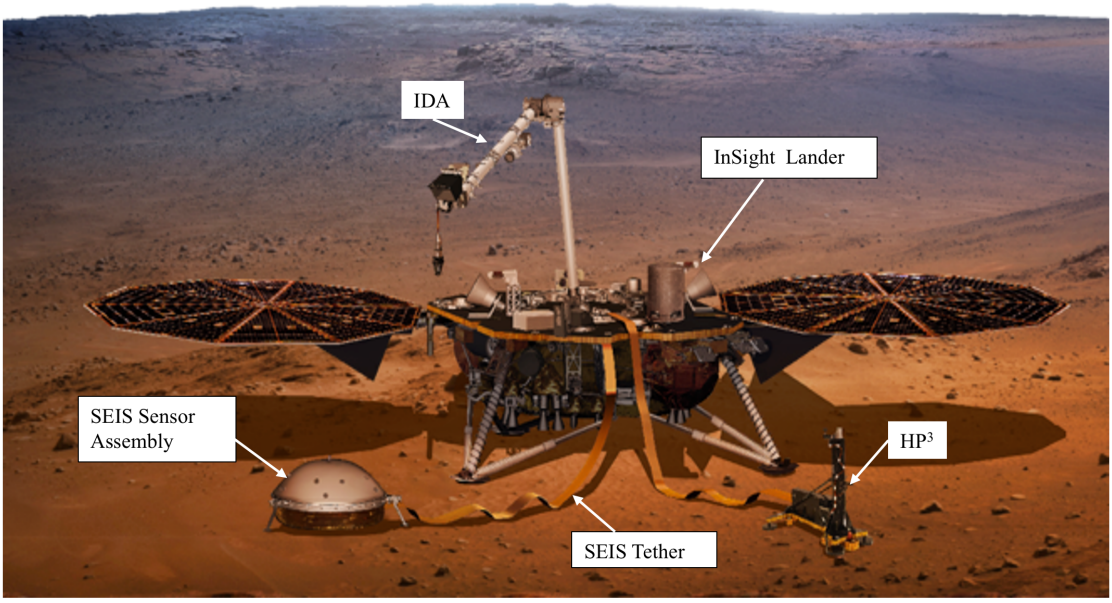

Figure 1. The InSight lander viewed from the south. (Artists conception) The seismic sensors in the Sensor Assembly receive power from, and send signals to, the SEIS electronics housed in the Lander, where they are kept much warmer, via the tether. The Heat Flow and Physical Properties Package (HP^3) experiment is on the ground to the right of SEIS, and the Instrument Deployment Arm (IDA) with attached Camera used to deploy both the SEIS Sensor Assembly and the HP^3 probe is above the lander.

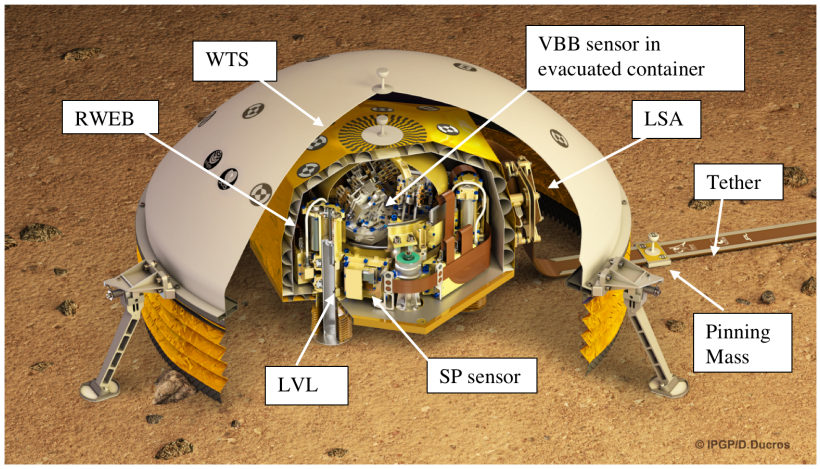

Figure 2. Cutaway view of the InSight seismometer sensor assembly on Mars. RWEB: double-walled thermal enclosure. WTS: Wind and Thermal Shield. LVL: One leveling leg (of 3) for the leveling and support structure. SP sensor: One of 3 SP sensors (this one is the vertical one). VBB sensor: One of 3 oblique VBB sensors inside the evacuated chamber. LSA: Load Shunt Assembly (shown prior to opening) to isolate the thermoelastic disturbances in the tether from the sensor assembly. Tether: A five-belt copper-on-Kapton flexible circuit connecting the sensor assembly to the electronics in the lander. PM: Pinning Mass helps isolate the thermoelastic disturbances in the tether from the sensor assembly, and provides a handle for adjusting the opening of the LSA.

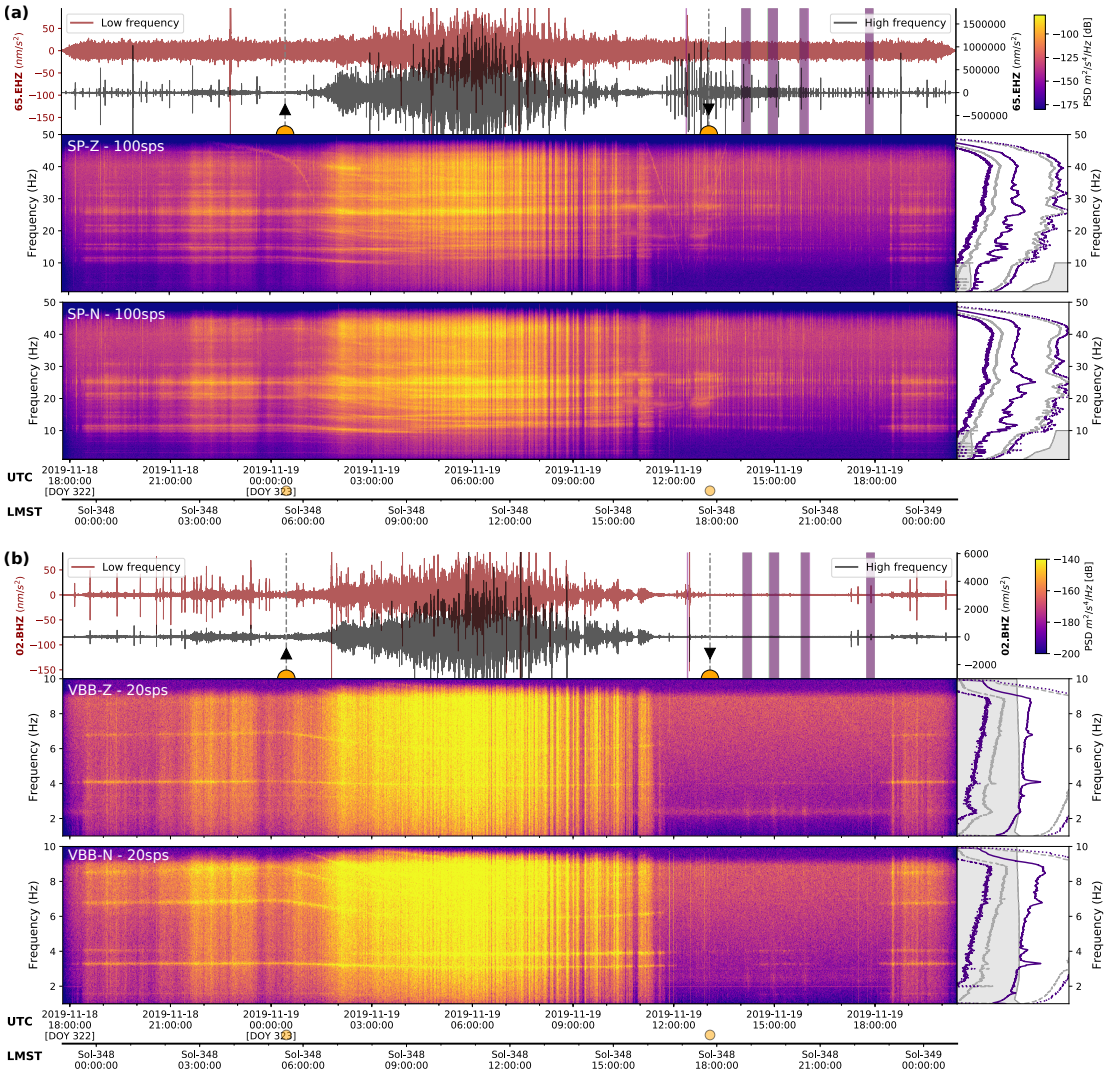

Figure 3. Example of typical data from Sol 348: vertical acceleration time series and vertical and north spectrograms from (a) 100 sps SP, and (b) 20 sps VBB. The x-axes at the bottom shows time in both UTC and Local Mean Solar Time on Mars as LMST. Sunrise and sunset are shown as orange hemispheres with arrows at the top of the panels,and as orange circles in the timescale at the bottom. To the right of the spectrograms are the probabilistic power spectral density. At the top, there are two filtered versions of the time series (above and below 1Hz). The strongest horizontal lines in the spectrogram between 2 and 10 Hz are traceable to the lander and are discussed in Ceylan et al. (2021). The many vertical "spikes" in (b) that appear to originate in the longest periods in the spectrogram are discussed in Scholz et al. (2020). The vertical purple bars in the waveform panels mark the duration of seismic events identified by the Marsquake Service Clinton et al. (2018).

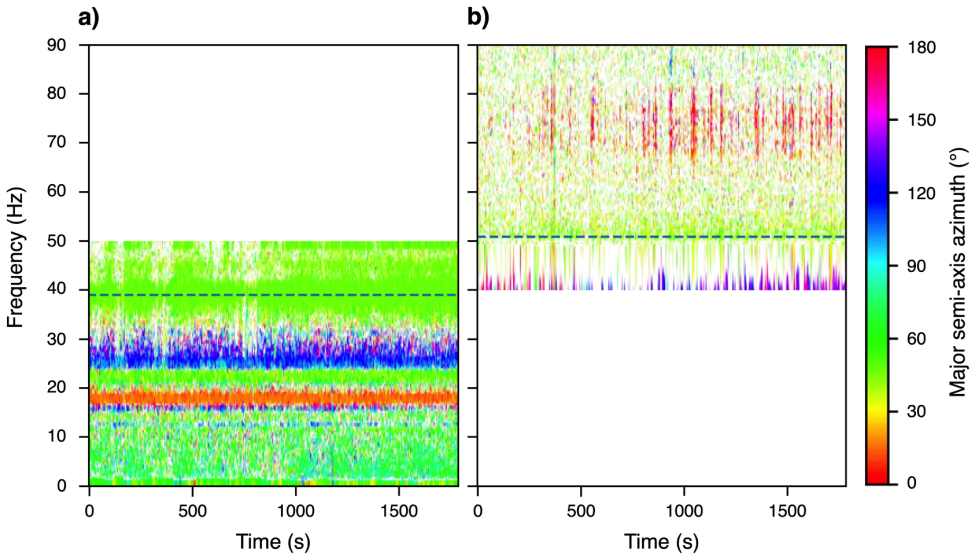

Figure 4. Display of the azimuth of the major axis of the polarization ellipse with frequency and time for wind induced noise for (a) Pre- and (b) post-leveling low of the LVL. The pre-leveling low LVL resonance at around 39 Hz was not as clearly visible as after leveling low, when the LVL resonance moved to 51 Hz, as suggested by the common azimuth of the pre- and post-leveling low resonances at around 60 degrees.

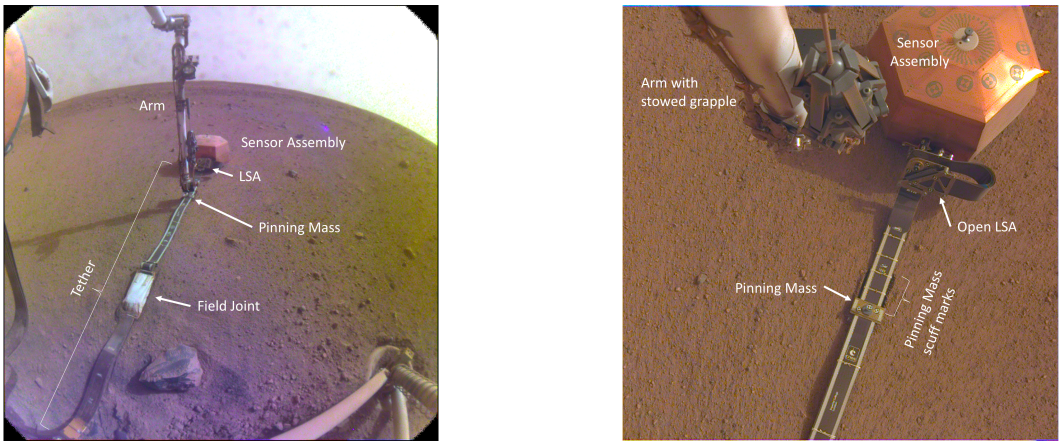

Figure 5. Context (left) and Deployment (right) Camera images of the last adjustment of the Pinning Mass to open the LSA. The shadow of the LSA in the Deployment image shows clearly that sunlight is able to shine all the way through, offering an additional avenue for assessing the proper state of the LSA opening.

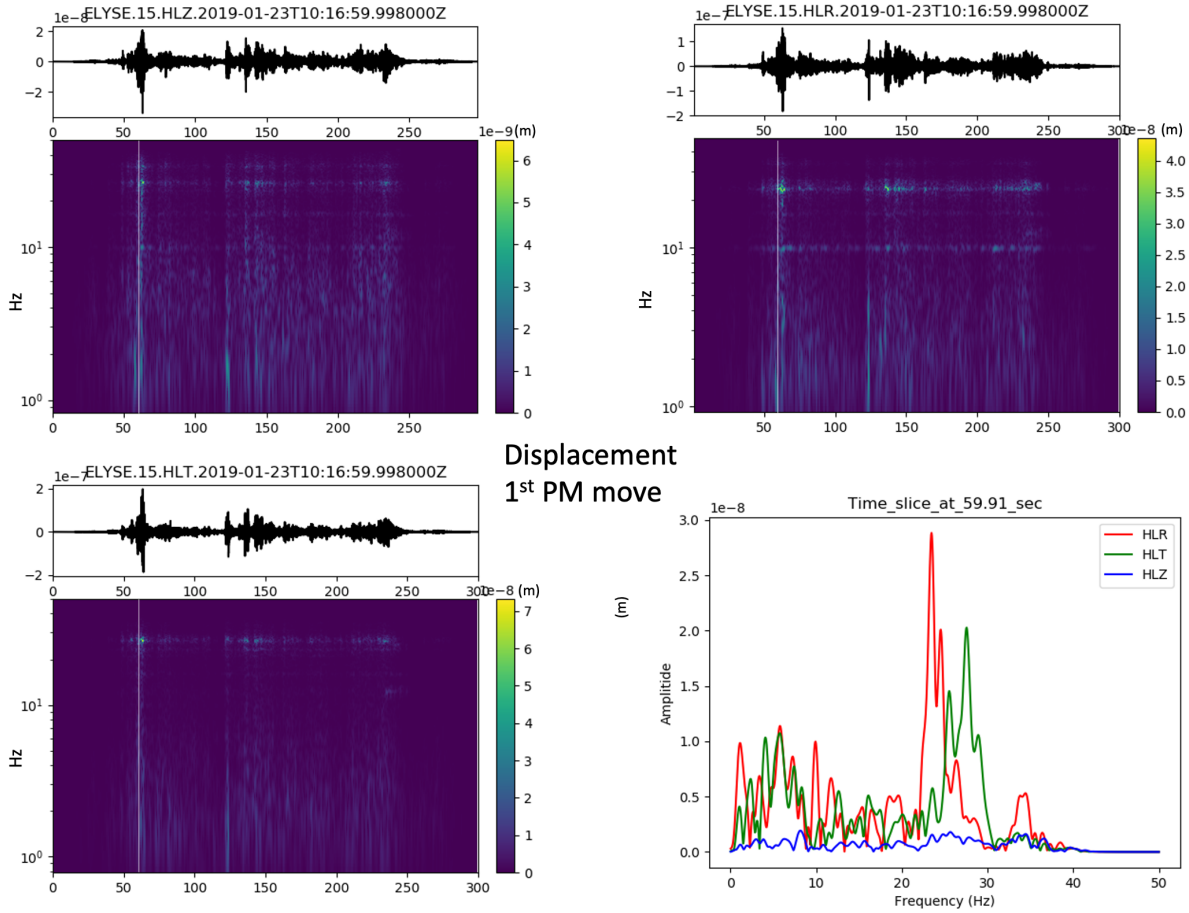

Figure 6. Spectra of the LSA on Mars as stimulated by the first Pinning Mass adjustment during deployment. This is applicable to the period from sol 44 (leveling low) to sol 59 (LSA open). R == radial with respect to the direction of the tether. T == transverse to the tether. Z == Vertical.

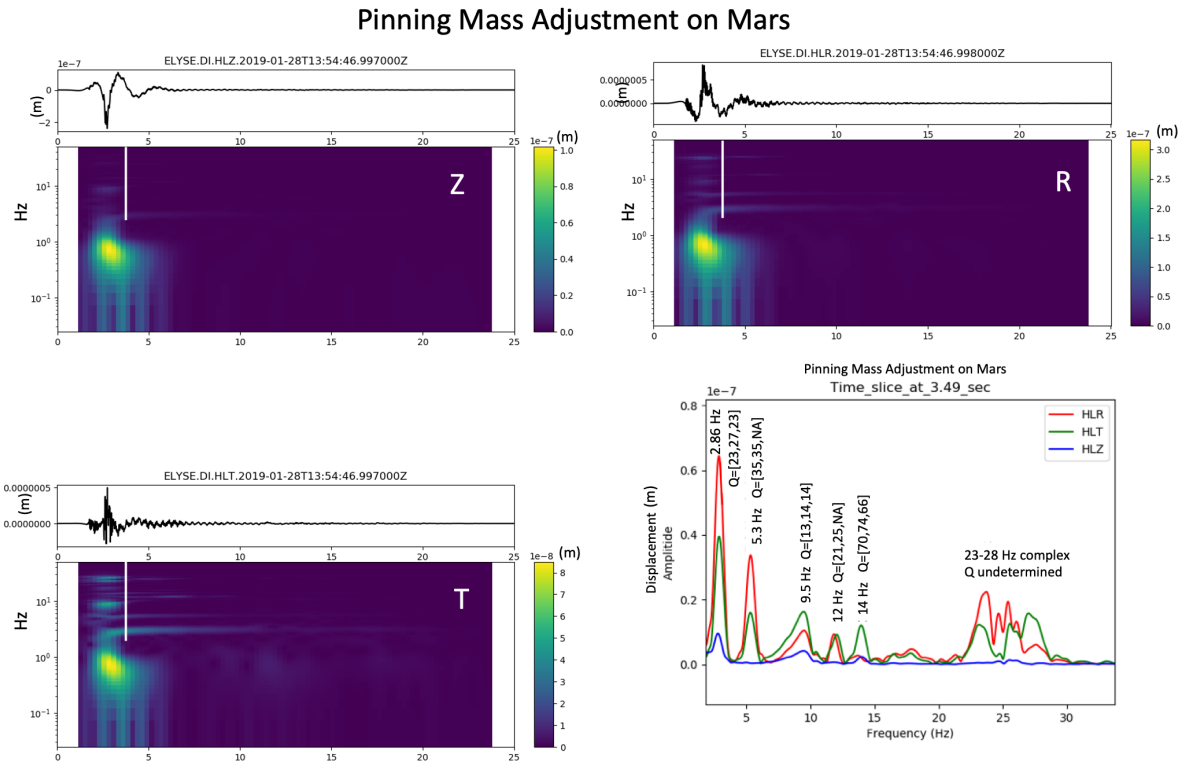

Figure 7. Spectrograms of the LSA on Mars as stimulated by the last Pinning Mass adjustment during deployment. The data was high-pass filtered with a cutoff at 0.5 Hz. This is applicable from sol 59 (LSA open) to the end of the mission. R == radial with respect to the direction of the tether. T == transverse to the tether. Z == Vertical. The spectrum on the bottom right corresponds to a slice through the spectrogram at the white line in each spectrogram.

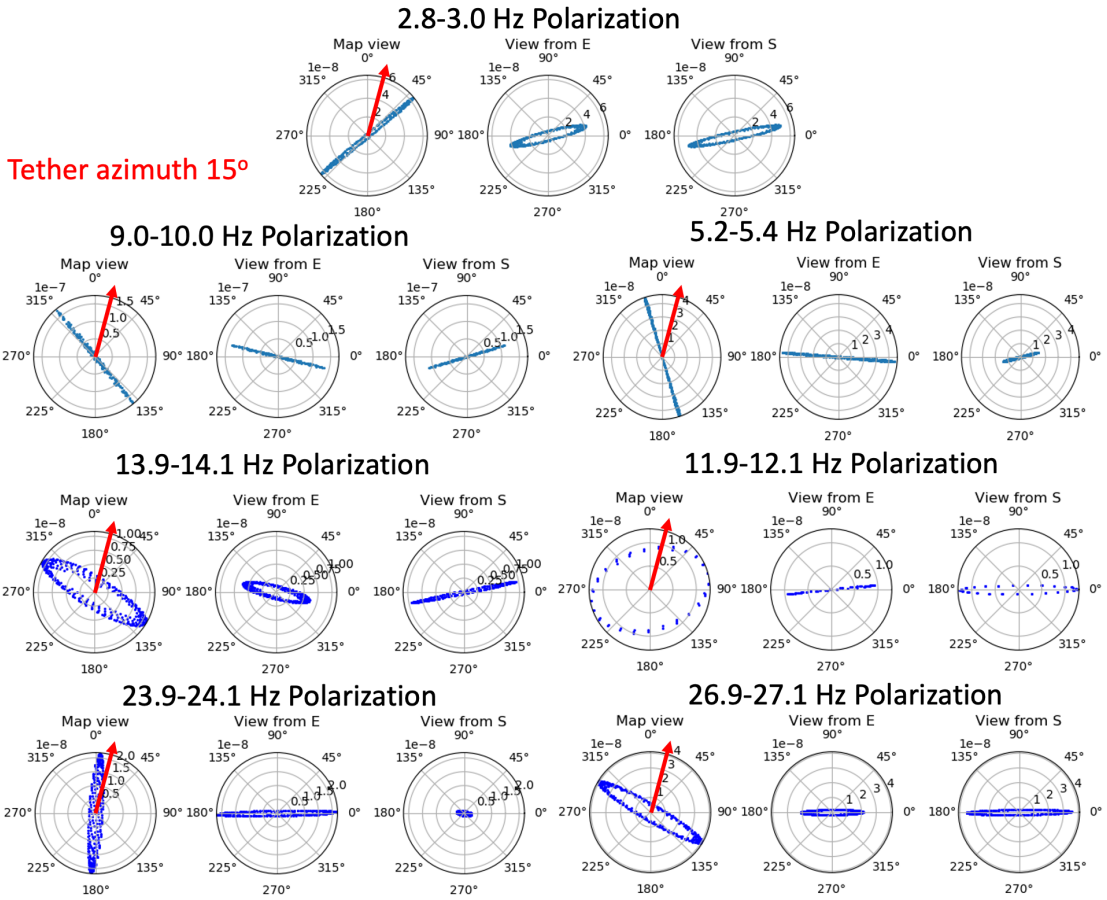

Figure 8. Polarization plots for the first 7 modes from the last pinning mass adjustment. The views are from 3 orthogonal viewpoints, with the left (map) view in map coordinates with North at 0°, and East at 90°. The middle plot is the N-V plane as viewed from the East, with up at 90°. And the right plot is the E-V plane as viewed from the South, again with up at 90°. The azimuth of the tether is at 15°and is indicated by the red arrows on the Map view plots. The narrow band-pass filters applied to isolate each mode are given in the titles for each set of plots.

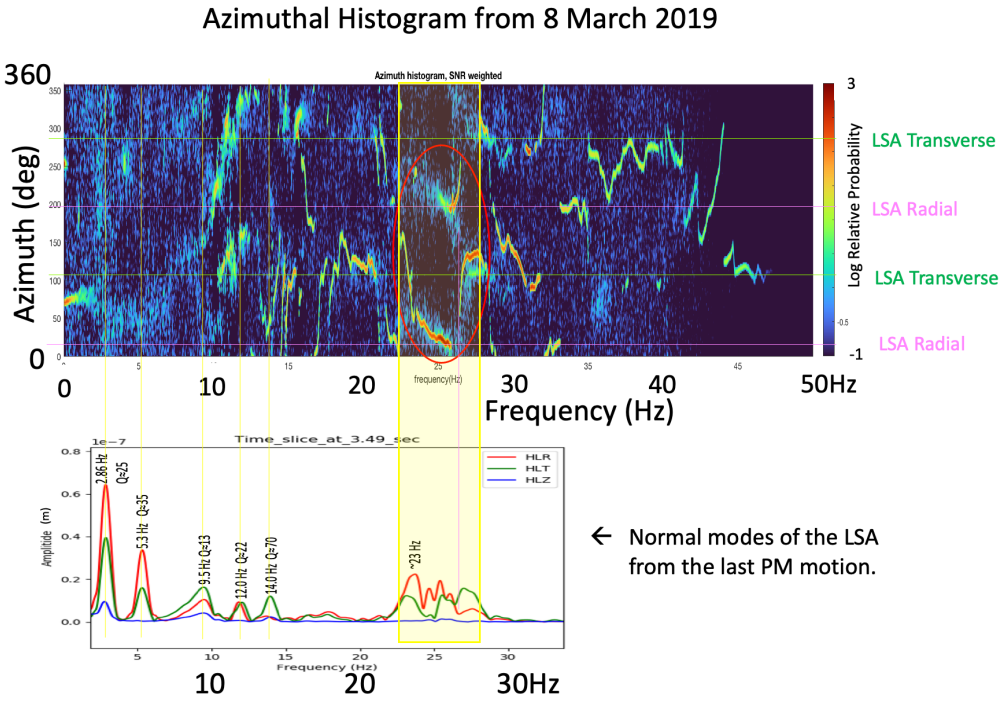

Figure 9. Azimuthal histogram of 5 minutes of 100sps SP data from 8 March 2019, demonstrating the effect of resonances in the LSA between 23 and 28 Hz.

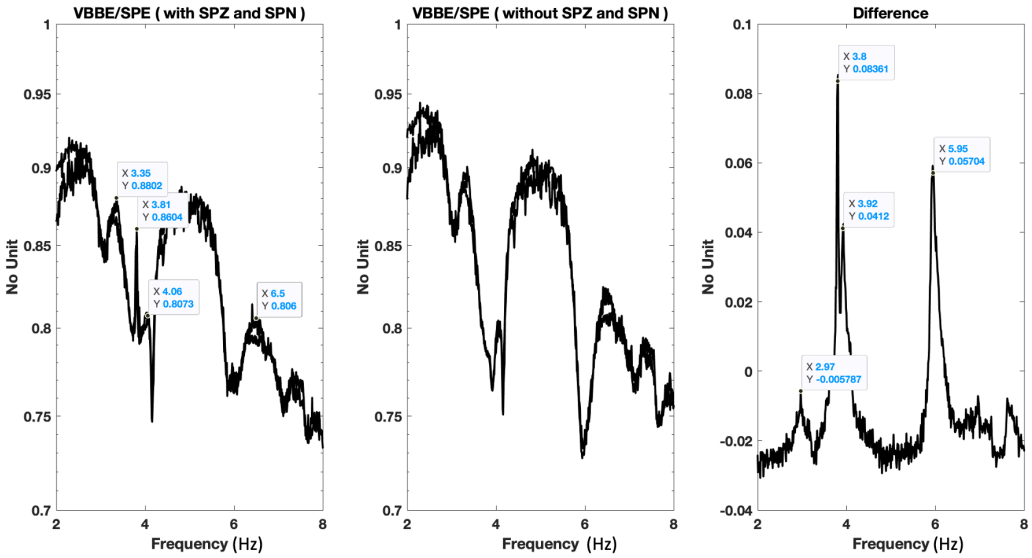

Figure 10. Residual from filtering the SP data to match the VBB data. In the left panel, all 3 SP components are used to create a filter to match the VBB-East component. In the central panel, only the SP-East component is used to create a filter to match the VBB-East component. The right panel shows the ratio between the east component of the 3-component filter, and the single component filter. This shows a minor peak at 2.97 Hz, about 0.1 Hz above the frequency measured during the last pinning mass adjustment.

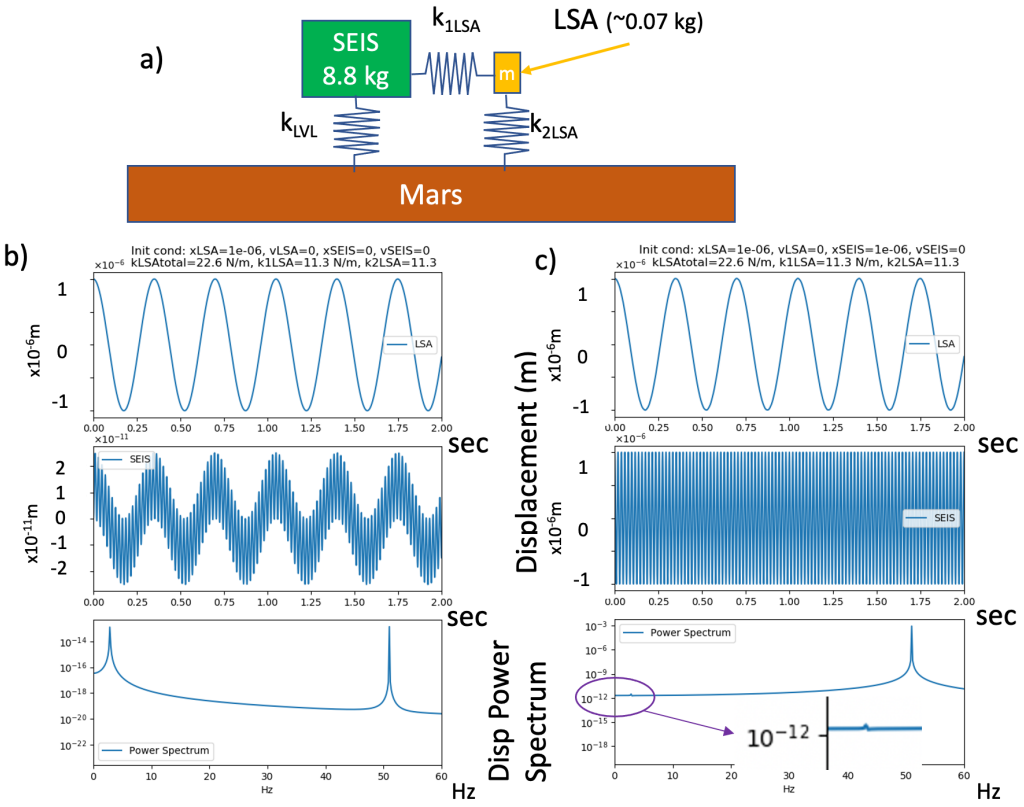

Figure 11. Coupled undamped harmonic oscillator model for SEIS Sensor Assembly and the LSA. a) A diagram of the model. b) Displacement response of the system to an initial displacement of only the LSA of 1.0e-6 m for the 2.86 Hz LSA resonance. c) Displacement response of the system to an initial displacement of **both** the Sensor Assembly and the LSA of 1.0e-6 m/s for the 2.86 Hz LSA resonance. The 2.86 Hz resonance can just be seen in the blowup in the PSD.

Supplemental Material

Supplement to Resonances of the InSight Seismometer on Mars

K. J. Hurst, **L. Fayon**, **B. Knapmeyer-Endrun**, **C. Schmelzbach**, **M. van Driel**, **J. Ervin**, **S. Kedar**, **W. Pike**, **M. Bierwirth**, **P. Lognonne**, **S. Ceylan**, **M. Böse**, **J. Clinton**, **D. Giardini**, **A. Horleston**, **T. Kawamura**, **A. Khan**, **G. Orhand-Mainsant**, **J.-R. Scholz**, **S. Stähler**, **J. Stevanovic**, **W. Banerdt**

Introduction

This supplement contains descriptions and results from analyses and tests done on Earth, either with an Engineering Model (EM) of the LVL with a Trillium Compact 120 seismometer taking the place of the VBBs and SPs.

Origin of LVL resonances

A simplified analytical model of the LVL structure has been developed in order to reproduce its mechanical behavior by predicting its resonances and transfer function (Fayon et al., 2018).

For any case of reasonable ground rigidity values tested in the model, two horizontal resonances were observed in the SEIS range of measurements, i. e. below 50 Hz, which is similar to the results of laboratory and field tests on Earth (see below).

This model has shown that the observed horizontal resonance frequencies are highly dependent on the elastic properties of the ground, i.e values of the Young's modulus and the Poisson's ratio. Indeed, a change of these values inside the model can make the resonance frequencies vary between approximately 20 and 100 Hz, depending on the fixed values of the other parameters. All modeling results are summarized in Figure S6 and indicate that the resonance frequencies primarily depend on the length of the legs and the interactions between the LVL's legs and the ground.

Tests on Earth

Test measurements conducted on Earth provided pre-flight indications of the expected LVL behavior on Mars. These included lab tests with different LVL versions in different stages of completeness of the assembly, as well as field tests with EMs. Lab tests were performed using both the forced excitation of a shaker and the ambient vibration background as a source (Fayon et al., 2018), whereas field tests used ambient sources (Knapmeyer-Endrun et al., 2018) and the hammering of a proto-flight equivalent model of the HP3 mole (Kedar et al., 2019).

Measurements done using ambient vibrations as a source were usually conducted using two seismometers of the same type, namely Nanometrics Trillium compact 120s, one on the LVL and one as a reference sensor situated on the ground less than two meters from the LVL, and thus subject to the same ambient ground motion. The resonance frequencies were determined by comparing the power spectral densities (PSD) of simultaneous recordings with both sensors, similar to the measurement principle commonly used in seismometer calibration (Pavlis and Vernon, 1994). Sharp resonance peaks were observed in the PSD for every measurement performed on the LVL.

All measurements exhibited a common behavior. In measurements covering a frequency range up to 100 Hz, resonances could only be observed on the horizontal components. For equal lengths of the LVL legs, a single resonance frequency was observed, whereas an LVL levelled on tilted ground resulted in two resonance peaks. Longer leg lengths as well as a higher mass of the LVL lead to a lowering of the resonance frequencies, as also predicted by the numerical model (Fayon et al., 2018).

All resonance frequencies measured for realistic deployment configurations, i.e. an LVL mass close to 9000 g and a leveling where at least one leg was close to its minimum extraction, were in the range of 35 to 46 Hz. As indicated by the numerical model, the coupling between the LVL feet and the ground also has an important influence on the resonance frequencies, though. The measurements conducted on Earth proved insufficient to study this influence, or support any firm conclusions on the effect of a hard floor versus a ground covered in sand on the frequency and amplitude of the LVL resonances. Based on the field measurements done on sand, however, the

damping ratio of the LVL resonances on Mars is expected to lie around 1%, corresponding to a Q around 50, with an even higher Q found for the measurements taken on a hard surface without sand cover (Knapmeyer-Endrun et al., 2018).

LSA: Testing on Earth

The influence of the open LSA on the EM LVL structure on Earth was assessed by stimulating the LSA either manually or with a device injecting a sinusoidal motion of the tether at the ground-contact point.

Manually stimulating the LSA

The first method of manual stimulation consisted of plucking the outer bracket of the LSA with a finger, and then analyzing the resulting "ring-down" as recorded on a Trillium Compact 120 seismometer (TC-120) sitting on top of the LVL. The experimental setup is shown in Figure S5. A TC-120 was placed on an aluminum plate at the center of the LVL structure. The seismometer power and signals were run through the tether and the open LSA and data was recorded at 200 sps on a RefTek RT-130 data recorder synchronized to GPS time.

The time series and spectra from two such experiments with different LVL leg configurations are shown in Figures S2 and S3. The frequencies remain similar between the two sets. The appearance of the relative amplitudes is largely a result of the time relative to the initial stimulation. The lower frequencies decay more slowly, so a spectrum taken a longer time after the initial stimulation will emphasize the lower frequencies. Both of these setups had the outer bracket of the LSA tilted with the top of the bracket away from the Sensor Assembly. On Mars the outer bracket is tilted with the top of the bracket toward the Sensor Assembly.

We also moved the Pinning Mass by hand and observed the resulting "ring-down" recorded on the TC-120 seismometer as seen in Figure S4. These two methods gave equivalent results as can be seen by comparing Figures S4 and S3 which shared the same setup.

In another experiment, we placed a small, lightweight accelerometer on the outboard (loose or

mobile) part of the LSA, another on the inboard (fixed) part of the LSA, both recording at 1000 sps and simultaneously recorded the acceleration on a TC-120 sitting on a plate on the LVL which was sitting in coarse sand. The TC-120 data was recorded on a RefTek 130 data recorder through a separate cable in contrast to other experiments where the TC-120 signals were run through the tether (and LSA). The resulting acceleration spectra are presented in Figure S8. We observe the three similar peaks at about 3, 5 and 10 Hz. By comparing the amplitude levels of the "loose" part of the LSA (green) and TC-120 (black), we can see that the acceleration (and therefore forces) are attenuated by factors of 10^4 to 10^5 at these LSA resonances, in rough agreement with the admittance derived from the tether moving experiment in Figure S9 discussed below and the simple spring and mass model discussed in the main paper.

Injecting a Sinusoid into the LSA

In order to quantify the efficacy of the LSA at isolating the seismometer from radial motions of the tether as a function of frequency, we clamped a device to the tether in the sandbox at roughly the location where the tether last touches the regolith simulant. The device moved the tether with a sinusoidal motion at frequencies that could be adjusted between 0.03 and 1 Hz, with an amplitude of about 0.4 mm. A picture of the setup showing the tether moving device is shown in Figure S5B.

Figure S9 shows the ratio of the displacement as measured by the seismometer to the displacement of the tether as measured by a capacitance gauge. The admittance plot on the right side of the figure shows that the transverse response is about 0.6 of the longitudinal response. We have not attempted to input transverse sinusoids or side-to-side rocking of the tether because the LSA was indended to decouple the thermoelastic expansion and contraction of the tether from the Sensor Assembly which is a radial motion. If one were to include wind-induced vibration of the tether, then transverse input would become important. Because the wind velocity goes to zero at the surface, and the tether is very close to the ground, and because of the very low density of the Martian atmosphere, we have not considered wind-induced vibrations here.

Transfer function based on Earth data

We computed a transfer function for a similar setup on Earth. We recorded a M5.5 earthquake 170 km away on both a Trillium Compact 120 seismometer sitting on the EM LVL structure which in turn was sitting in a 10 cm deep sandbox sitting on the JPL seismic pier, with an adjacent STS-2 also sitting on the pier. The setup is shown on the left side of Figure S10. Both seismometers were sampling at 200 sps with 24 bit resolution. The sandbox had no bottom, and was lined with a plastic sheet then filled with 10 cm of MMS-2 regolith simulant (Peters et al., 2008). The LSA was open and configured similarly to the LSA on Mars.

The leg lengths of the EM LVL were as shown in the table in the bottom left of Figure S10. The two seismometers were aligned in azimuth by maximizing their cross-correlation and rotated such that the radial direction is along the tether, Z is up, and transverse completes a right-handed RTZ system.

The acceleration spectra and transfer function for 0.03 - 50 Hz is shown in Figure S10. The extension of the transfer function beyond the required frequency band (0.1-1 Hz for horizontal and 0.01-1 Hz for vertical) will be useful for understanding the Martian seismicity which is recorded in the 0.1-8 Hz band and for the high frequency experiments using the HP^3 mole hammer strokes as a seismic source. The transfer function shows the effect of the LSA resonances in the 3-20 Hz range and the LVL resonance in the horizontal components at about 39 Hz. This LVL resonance is moved up to 51 Hz for the installation on Mars due to 1) shorter leg lengths, and 2) less mass.

The transfer function is well approximated by a value of 1 over the required 0.01-1.0 Hz band for the vertical component, and over the 0.1-1.0 Hz band for the radial and transverse (WRT the direction of the tether) components.

Supplemental Tables

Table S1: Leg lengths for the three LVL legs as deployed on Mars, compared to the closest test configuration for which resonances were measured on Earth. The length is measured between the bottom of the LVL ring and the top of the foot flange.

Leg No.	Leg Length on Mars (mm)	Leg Length on Earth (mm)
1	54.7	54.2
2	59.3	60.5
3	49.5	53.4

List of supplemental figure captions

Figure S1: Gain of the relative transfer function between a sensor located on the LVL and one located on the floor close-by, determined from 6 hours of ambient noise measurements in the lab.

Figure S2: The "ring down" recorded from a finger plucking the open LSA for one of two different setups of the LSA. (data collected on Earth) The spectra plots are located within their respective spectrograms as shown by the vertical white lines. The details of the setup geometry are in the table at the bottom, where the 3 leg lengths, the opening of the LSA at the top, the angle of the outer bracket with respect to vertical (degrees) the distance from the inner bracket to the first contact with the ground, the pitch (+ up along tether to SA), and the roll are given. (Note that the sand surface was not planar and changed over time, so the leg length differences can not be used to infer the difference in tilt of the sandbox.)

Figure S3: The "ring down" recorded from a finger plucking the open LSA for the second of two different setups of the LSA. (data collected on Earth) Note change in color scheme from the spectra plots in S2. The spectra plots are located within their respective spectrograms as shown by the vertical white lines. The details of the setup geometry are in the table at the bottom, where the 3 leg lengths, the opening of the LSA at the top, the angle of the outer bracket with respect to vertical (degrees) the distance from the inner bracket to the first contact with the ground, the pitch (+ up along tether to SA), and the roll are given. (Note that the sand surface was not planar and changed over time, so the leg length differences can not be used to infer the difference in tilt of the sandbox.)

Figure S4: Resonances as observed during a static adjustment of the Pinning Mass for the Earth-bound setup in Figure S3

Figure S5: Sandbox setup. A) The STS-2 reference seismometer was sitting on the bottom of the sandbox in the far corner. A Trillium Compact TC-120 seismometer was placed on top of an adapter plate in the center of the Engineering Model LVL system which was sitting on Mojave Mars Simulant (MMS-2) Peters et al. (2008) about 12 cm deep. The electrical connections to the TC-120 were run through the tether. B) The picture on the right shows how the tether mover

was clamped on the tether just outboard of the LSA and moved it in a sinusoidal manner with an amplitude of about 0.4mm (8mm p-p.)

Figure S6: Sensitivity of both modeled horizontal LVL resonance frequencies to the values of the ground elastic properties, i.e. the Poisson ratio in blue, the Young Modulus in red and the vertical stiffness of the ground material in contact with the LVL's feet in green.

Figure S7: Power spectral densities computed over 4 hours of data measured on Volcano island for the vertical (Z) and horizontal (X,Y) component velocity data. Red lines refer to the reference sensor placed on the ground, whereas the blue lines correspond to the contemporaneous measurements conducted on the LVL. Gray lines indicate the high and low noise models according to Peterson (1993)

Figure S8: Setup and results of instrumentation of a Twang test. Small accelerometers were glued to the LSA at the "Fixed" and "Loose" locations indicated. The loose side of the LSA was then plucked with a finger, generating the response shown. The accelerometer at the "Fixed" location shows no response (red) to the movement of the "Loose" side of the LSA because the motion is below the detection threshold of the accelerometer. The response is seen clearly in the more sensitive Trillium (black). At the LSA resonance frequencies of 3-10 Hz, the response is attenuated by 10^4 to 10^5

Figure S9: Displacement amplitude admittance for movements of the tether along the direction of the tether from an experiment on Earth with the EM LVL in a sandbox. On the top is an example time series showing several of the lowest-frequency sinusoidal motions that were imparted to the tether at the entrance to the LSA as shown in Figure S5B. The top panel is the motion of the tether at the clamp just outside the LSA, and the seismometer displacement response is in the following 3 panels. The frequency bandwidth where the SEIS horizontal (or vertical) noise performance requirement is specified is indicated in purple (or green) in the admittance plot on the bottom.

Figure S10: Acceleration transfer function between Trillium Compact seismometer on top of a LVL structure with an open LSA sitting in Mars regolith simulant, and an STS-2 sitting on the same seismic pier. The signal is provided by an M5.5 earthquake 170 km away. A picture of the

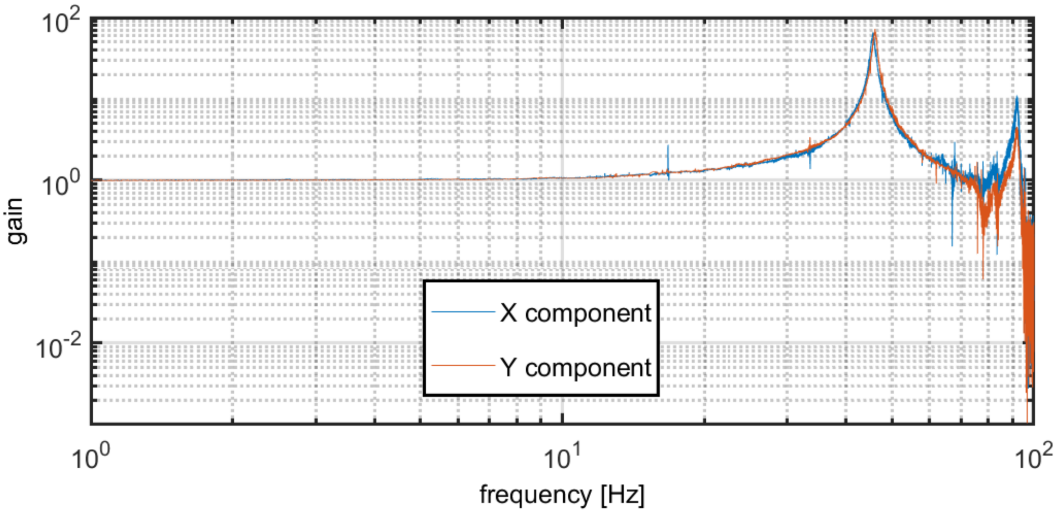

Figure S1. Gain of the relative transfer function between a sensor located on the LVL and one located on the floor close-by, determined from 6 hours of ambient noise measurements in the lab.

setup is shown on the left. Spectra of the acceleration for the Trillium and the STS-2 are shown at the top. The acceleration transfer function amplitude and phase are on the right. The leg extensions (LVL ring to foot flange) is given at the lower left (compare to table S1).

Supplemental Figures

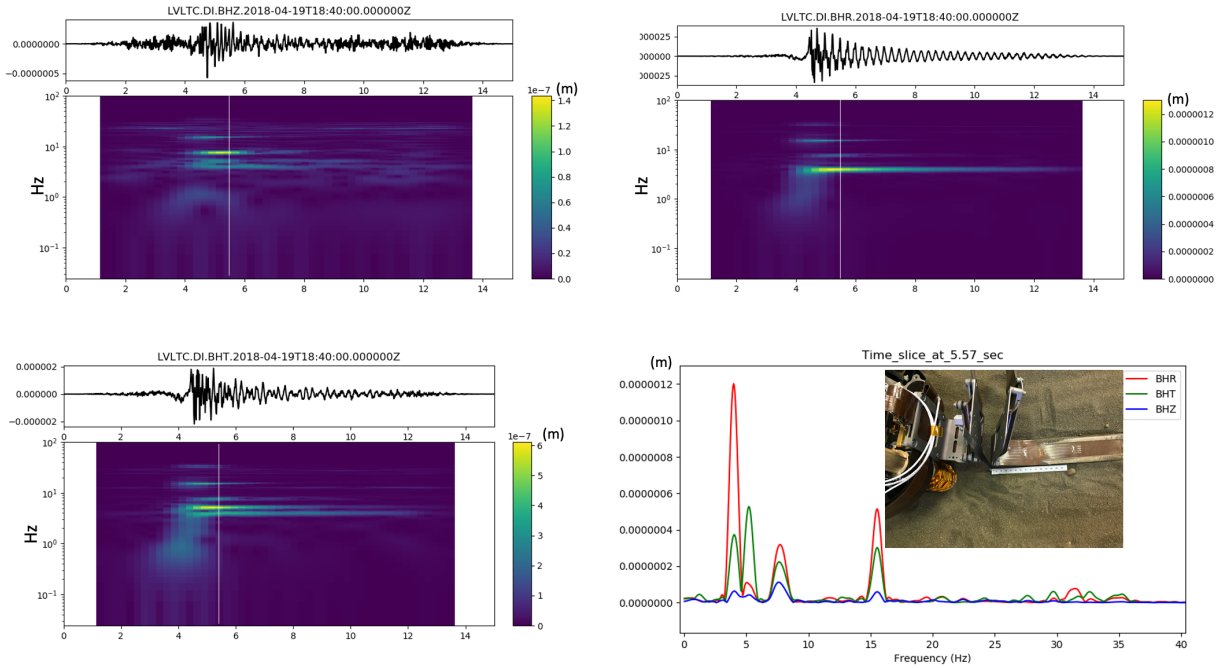

Leg1	Leg2	Leg3	LSA TopRight	LSA TopLeft	LSA V sep	LSA V angle	Grnd Dist	pitch	roll
65.8	56.5	55.5	40.6	40.5	-4	8	114	0	0

Figure S2. The "ring down" recorded from a finger plucking the open LSA for one of two different setups of the LSA. (data collected on Earth) The spectra plots are located within their respective spectrograms as shown by the vertical white lines. The details of the setup geometry are in the table at the bottom, where the 3 leg lengths, the opening of the LSA at the top, the angle of the outer bracket with respect to vertical (degrees) the distance from the inner bracket to the first contact with the ground, the pitch (+ up along tether to SA), and the roll are given. (Note that the sand surface was not planar and changed over time, so the leg length differences can not be used to infer the difference in tilt of the sandbox.)

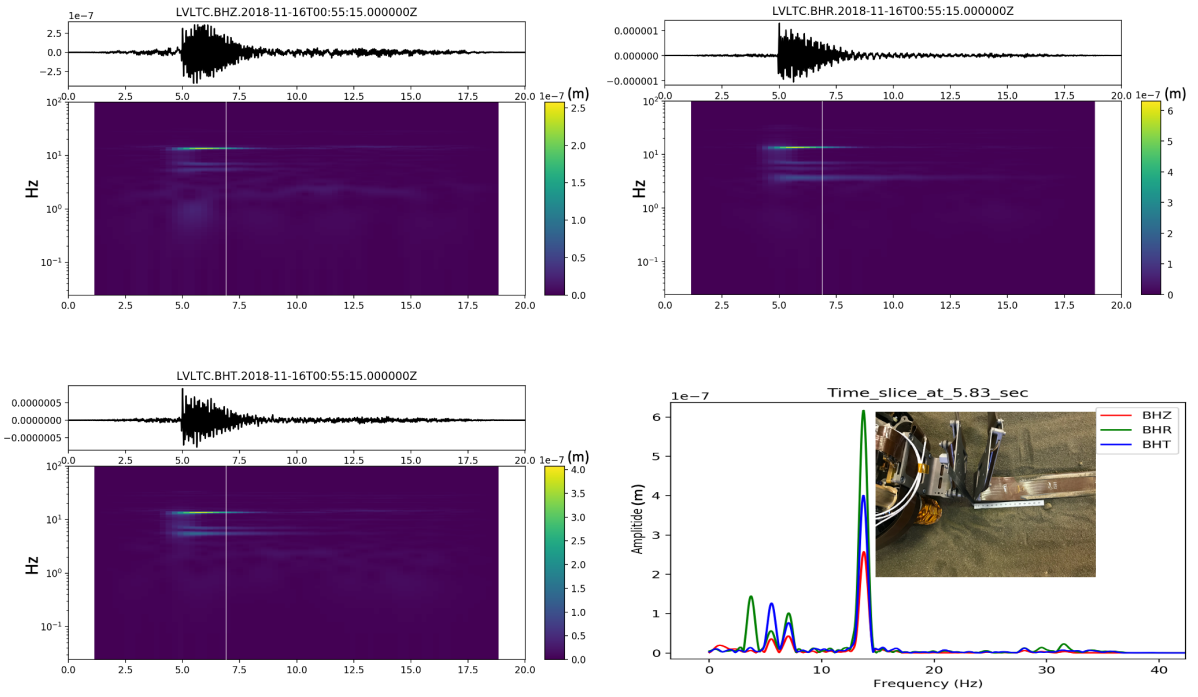

Leg1	Leg2	Leg3	LSA TopRight	LSA TopLeft	LSA V sep	LSA V angle	Grnd Dist	pitch	roll
82.9	85.8	82.2	23	22.6	28	6.2	90	-10	0

Figure S3. The "ring down" recorded from a finger plucking the open LSA for the second of two different setups of the LSA. (data collected on Earth) Note change in color scheme from the spectra plots in S2. The spectra plots are located within their respective spectrograms as shown by the vertical white lines. The details of the setup geometry are in the table at the bottom, where the 3 leg lengths, the opening of the LSA at the top, the angle of the outer bracket with respect to vertical (degrees) the distance from the inner bracket to the first contact with the ground, the pitch (+ up along tether to SA), and the roll are given. (Note that the sand surface was not planar and changed over time, so the leg length differences can not be used to infer the difference in tilt of the sandbox.)

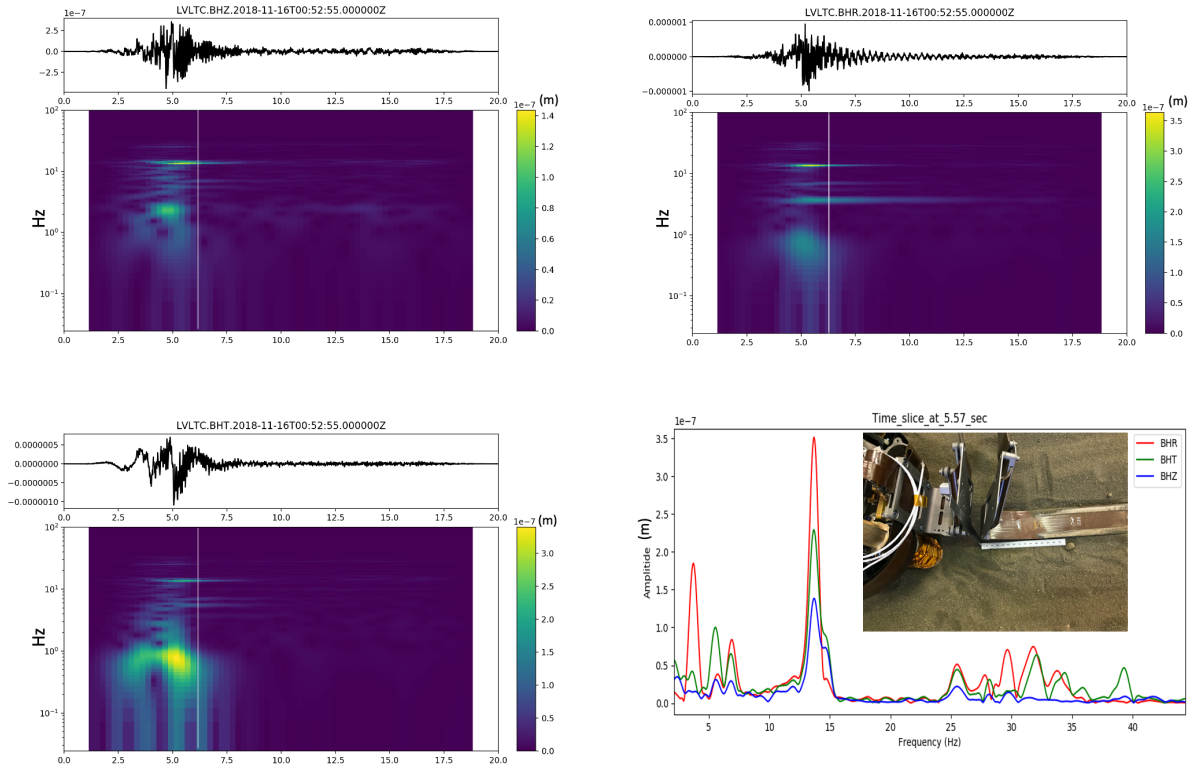

Leg1	Leg2	Leg3	LSA TopRight	LSA TopLeft	LSA V sep	LSA V angle	Grnd Dist	pitch	roll
82.9	85.8	82.2	23	22.6	28	6.2	90	-10	0

Figure S4. Resonances as observed during a static adjustment of the Pinning Mass for the Earth-bound setup in Figure S3

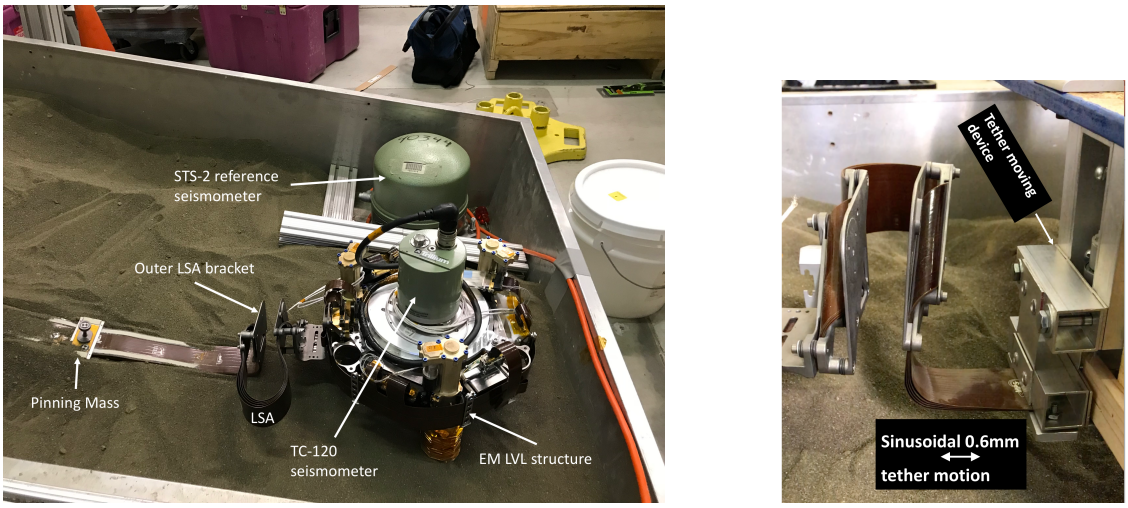

Figure S5. Sandbox setup. A) The STS-2 reference seismometer was sitting on the bottom of the sandbox in the far corner. A Trillium Compact TC-120 seismometer was placed on top of an adapter plate in the center of the Engineering Model LVL system which was sitting on Mojave Mars Simulant (MMS-2) Peters et al. (2008) about 12 cm deep. The electrical connections to the TC-120 were run through the tether. B) The picture on the right shows how the tether mover was clamped on the tether just outboard of the LSA and moved it in a sinusoidal manner with an amplitude of about 0.4mm (8mm p-p.)

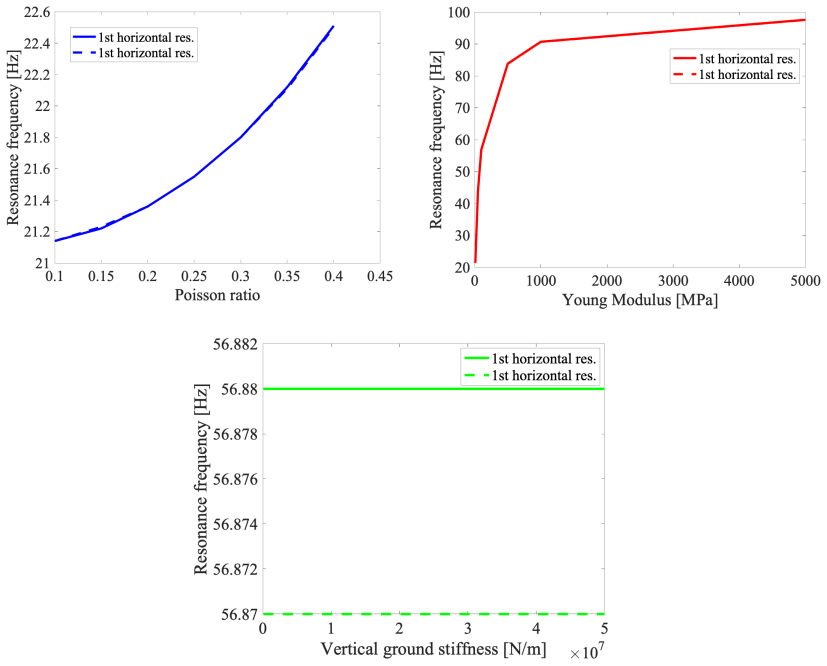

Figure S6. Sensitivity of both modeled horizontal LVL resonance frequencies to the values of the ground elastic properties, i.e. the Poisson ratio in blue, the Young Modulus in red and the vertical stiffness of the ground material in contact with the LVL's feet in green.

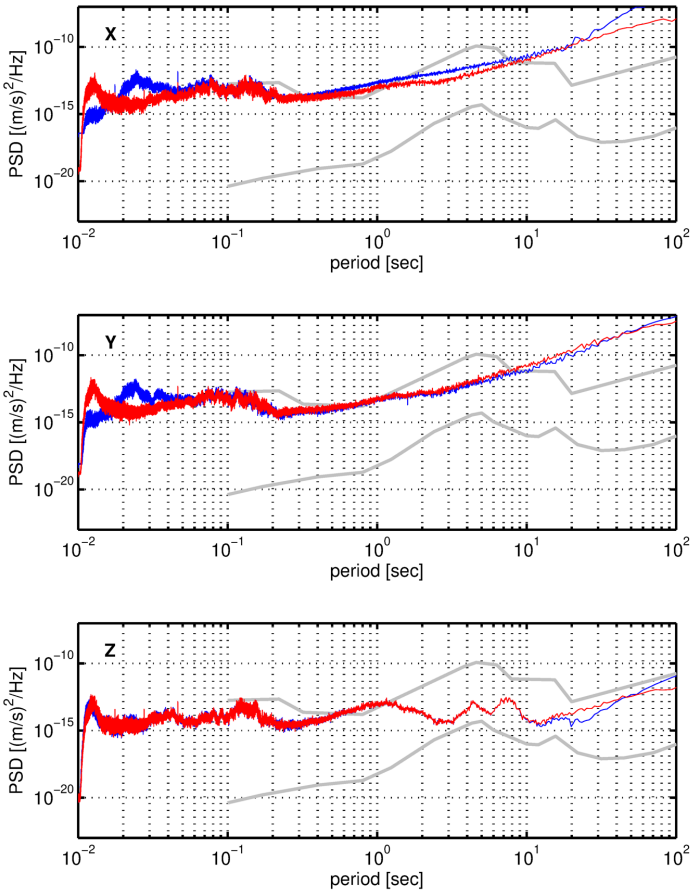

Figure S7. Power spectral densities computed over 4 hours of data measured on Volcano island for the vertical (Z) and horizontal (X,Y) component velocity data. Red lines refer to the reference sensor placed on the ground, whereas the blue lines correspond to the contemporaneous measurements conducted on the LVL. Gray lines indicate the high and low noise models according to Peterson (1993)

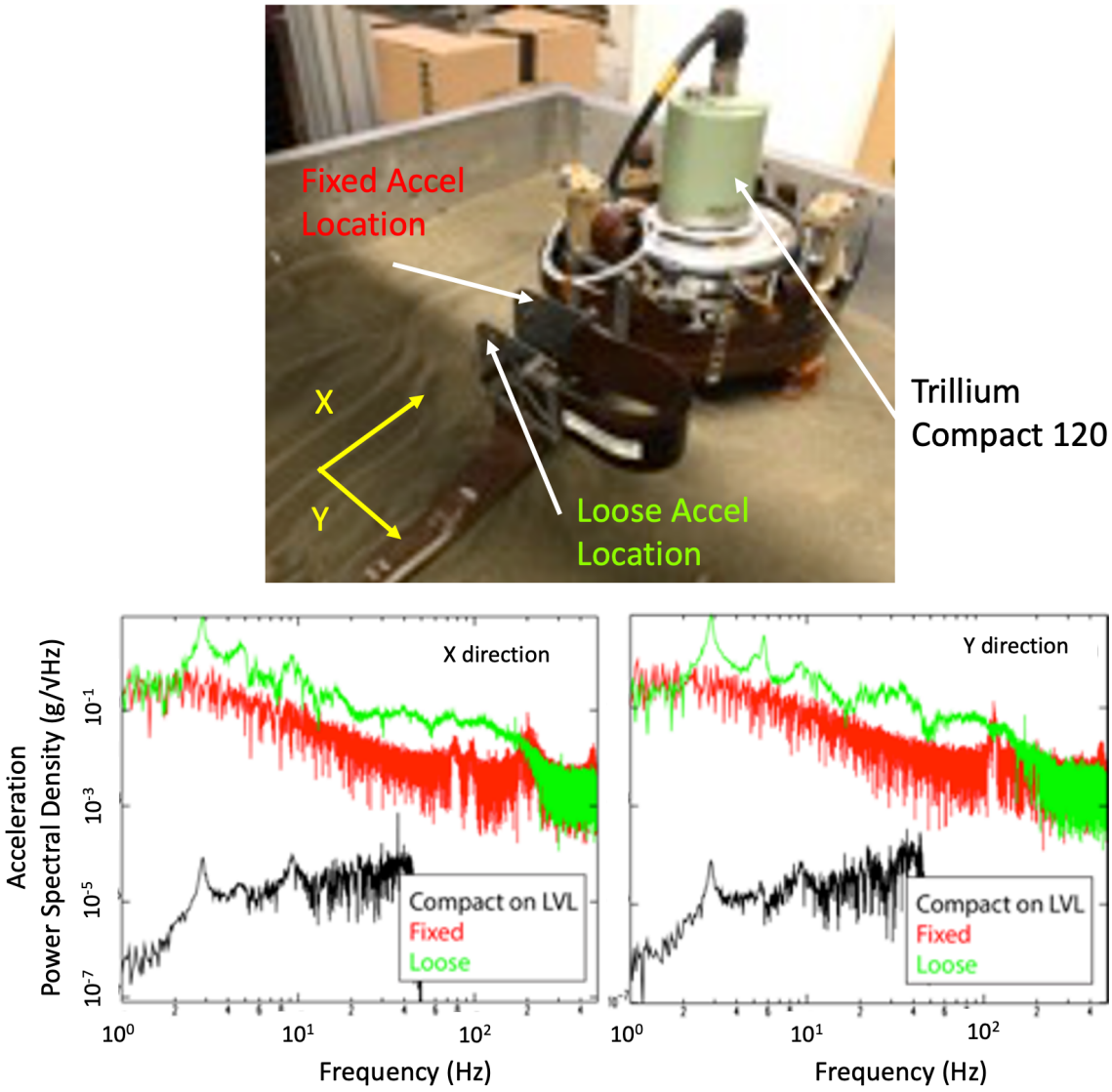

Figure S8. Setup and results of instrumentation of a Twang test. Small accelerometers were glued to the LSA at the "Fixed" and "Loose" locations indicated. The loose side of the LSA was then plucked with a finger, generating the response shown. The accelerometer at the "Fixed" location shows no response (red) to the movement of the "Loose" side of the LSA because the motion is below the detection threshold of the accelerometer. The response is seen clearly in the more sensitive Trillium (black). At the LSA resonance frequencies of 3-10 Hz, the response is attenuated by 10^4 to 10^5

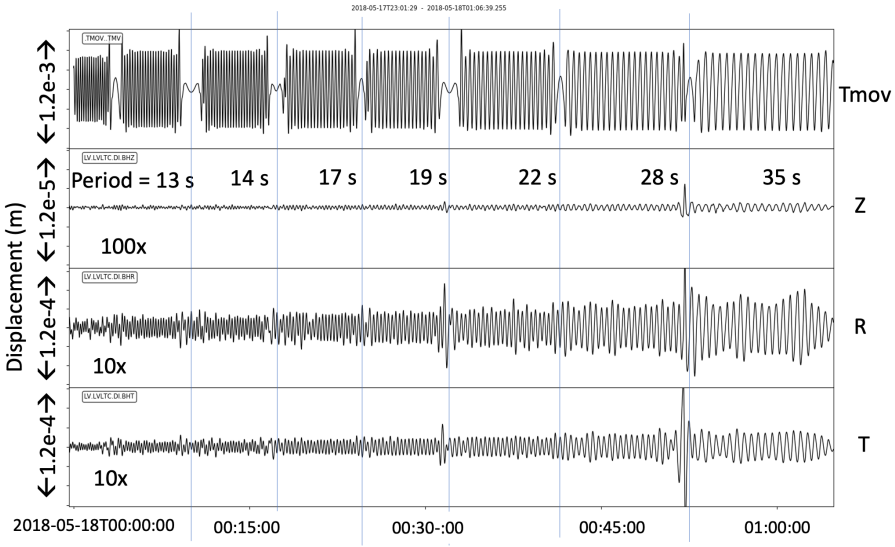

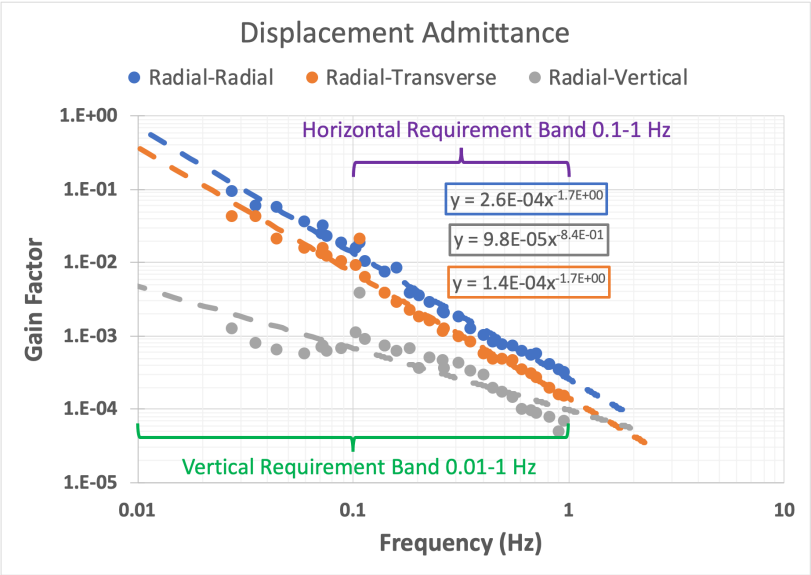

Figure S9. Displacement amplitude admittance for movements of the tether along the direction of the tether from an experiment on Earth with the EM LVL in a sandbox. On the top is an example time series showing several of the lowest-frequency sinusoidal motions that were imparted to the tether at the entrance to the LSA as shown in Figure S5B. The top panel is the motion of the tether at the clamp just outside the LSA, and the seismometer displacement response is in the following 3 panels. The frequency bandwidth where the SEIS horizontal (or vertical) noise performance requirement is specified is indicated in purple (or green) in the admittance plot on the bottom.

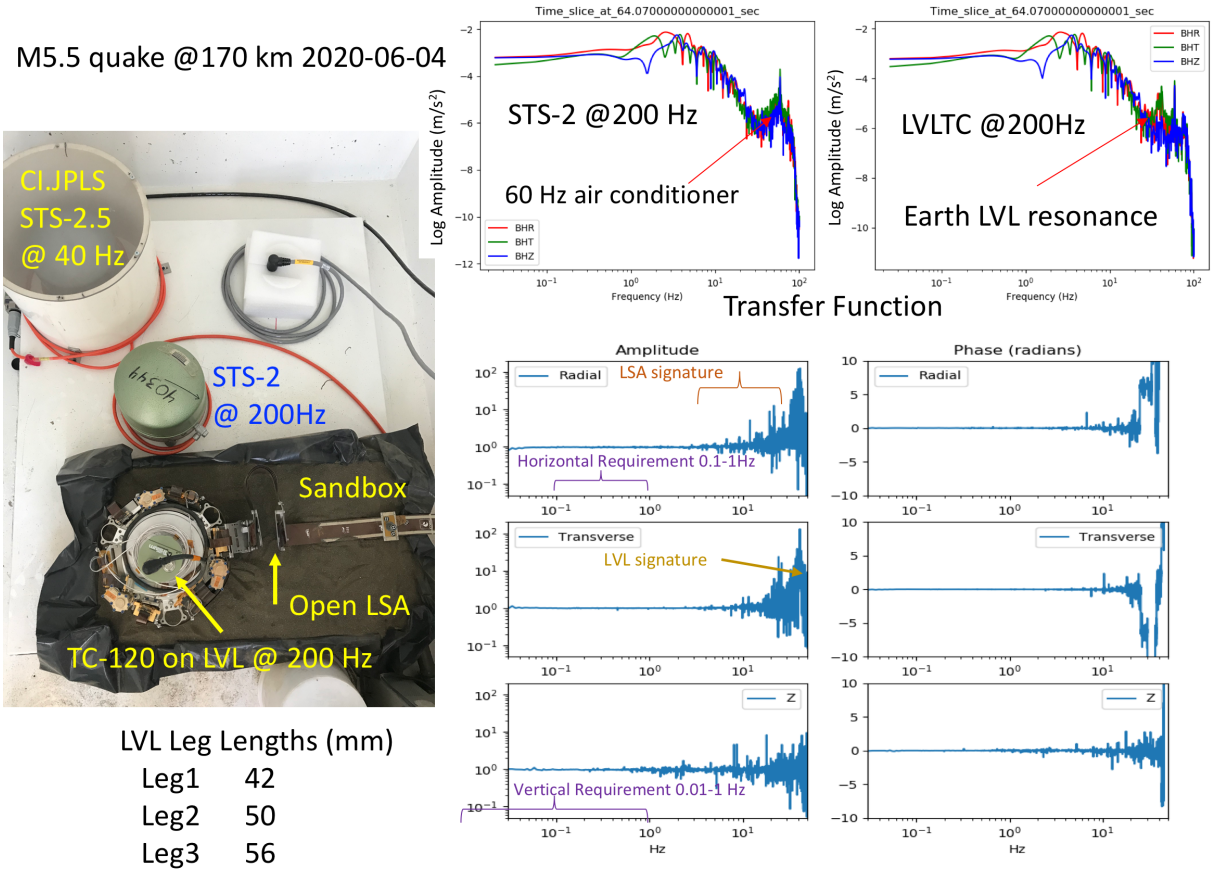

Figure S10. Acceleration transfer function between Trillium Compact seismometer on top of a LVL structure with an open LSA sitting in Mars regolith simulant, and an STS-2 sitting on the same seismic pier. The signal is provided by an M5.5 earthquake 170 km away. A picture of the setup is shown on the left. Spectra of the acceleration for the Trillium and the STS-2 are shown at the top. The acceleration transfer function amplitude and phase are on the right. The leg extensions (LVL ring to foot flange) is given at the lower left (compare to table S1).